High-resolution spectroscopy of barium monofluoride: Odd isotopologues, hyperfine structure, and isotope shifts

Felix Kogel [1], Yuly Chamorro [2], Mangesh Bhattarai [3,4], Marian Rockenhäuser [1,5], Tatsam Garg [1,5], David DeMille [3,4,6], Anastasia Borschevsky [2], and Tim Langen [1,5,*]

[1] *5. Physikalisches Institut and Center for Integrated Quantum Science and Technology, Universität Stuttgart, Pfaffenwaldring 57, 70569 Stuttgart, Germany*

[2] *University of Groningen, 9747AG Groningen, The Netherlands*

[3] *Department of Physics, University of Chicago, Chicago, Illinois 60637, USA*

[4] *Physics Division, Argonne National Laboratory, Lemont, Illinois 60439, USA*

[5] *Vienna Center for Quantum Science and Technology, Atominstitut, TU Wien, Stadionallee 2, 1020 Vienna, Austria*

[6] *Department of Physics and Astronomy, Johns Hopkins University, Baltimore, Maryland 21218, USA*

(Received 3 July 2025; accepted 2 September 2025; published 9 October 2025)

Barium monofluoride (BaF) is a promising molecular species for precision tests of fundamental symmetries and interactions. We present a combined theoretical and experimental study of BaF spectra and isotope shifts, focusing in particular on the poorly understood odd isotopologues ^{137}BaF and ^{135}BaF. By comparing state-of-the-art *ab initio* calculations with high-resolution fluorescence and absorption spectroscopy data, we provide a benchmark for electronic structure theory and disentangle the hyperfine and rovibrational spectra of the five most abundant isotopologues, from ^{138}BaF to ^{134}BaF. The comprehensive knowledge gained enables a King plot analysis of the isotope shifts that reveals the odd-even staggering of the barium nuclear charge radii. It also paths the way for improved laser cooling of rare BaF isotopologues and crucially supports future measurements of nuclear anapole and Schiff moments.

DOI: 10.1103/rdpt-99qy

I. INTRODUCTION

Molecules have recently been established as powerful precision sensors for the behavior of fundamental particles and interactions [1,2]. Their internal structure makes them highly sensitive to the effects of a hypothetical electron electric dipole moment [3–5], nuclear Schiff and magnetic quadrupole moments [6,7], and the variation of fundamental constants [8–13]. Moreover, their spectra can be sensitive to the shape and size of the nuclear charge and magnetization distributions [14–16], and molecules containing nuclei with unpaired nuclear spins can be used to probe nuclear-spin-dependent parity violation, anapole or Schiff moments [17–19].

It is also highly desirable to further increase the sensitivity of such measurements using laser cooling [20–23], and, recently, progress in this direction has been made for many molecular species [24,25]. Notably, the detailed spectroscopic information required to enable laser cooling is closely linked to the knowledge needed to carry out precision measurements for the fundamental physics goals. In turn, successful laser cooling can dramatically enhance spectroscopic sensitivity by increasing interrogation times and reducing thermal broadening.

The list of species that are both sensitive to fundamental physical effects of interest and suitable for laser cooling includes barium monofluoride (BaF), where high-resolution spectroscopy [26] has enabled the realization of optical cycling [27,28], low noise detection [26], Sisyphus laser cooling [29,30], and magneto-optical trapping of the most abundant isotopologue ^{138}BaF [31], as well as laser cooling of the rarer isotopologues ^{136}BaF [32] and ^{137}BaF [33]. BaF is distinguished by the existence of a total of five isotopologues with abundance greater than 1%, which show significant enhancements for searches for the electron electric dipole moment [23,34] and parity violation [17,35]. The barium nuclei in certain unstable isotopologues are also expected to exhibit significant octupole deformations [36], which may enhance sensitivity to Schiff moments arising from charge-parity-violating hadronic physics [37]. These observations collectively establish BaF as a compelling platform for exploring a wide range of fundamental phenomena via spectroscopy.

However, while the most abundant, even isotopologues of BaF have previously been studied extensively [26,38–41], precise knowledge about the odd—or fermionic—isotopologues of BaF, and in particular their hyperfine structure, has remained scarce [42,43], rendering the interpretation of spectra and assignments of lines of all isotopologues, including even ones with low abundance, challenging. This missing knowledge has, for example, limited achievable laser cooling forces for ^{137}BaF [30,33] and

*Contact author: tim.langen@tuwien.ac.at

leaves the transition frequencies of short-lived isotopologues poorly constrained and uncertain.

Here we systematically study the chain of stable BaF isotopologues from ^{134}BaF to ^{138}BaF using both fluorescence and absorption spectroscopy. We support our experimental results obtained in two independent and complementary experimental setups with state-of-the-art *ab initio* calculations of the excited-state hyperfine structure of the odd isotopologues, allowing us to benchmark such calculations and to reliably assign a large number of transitions. This enables us to systematically explore the isotope shifts in the BaF molecule with high precision using a King plot analysis. Our observations reveal the odd-even staggering of the nuclear charge radius of the barium atom, as we move from isotopes with odd numbers of neutrons to isotopes with even numbers of neutrons. Moreover, the extracted information provides important spectroscopic input for laser cooling and efficient detection of the odd isotopologues of barium monofluoride [44], which will be important ingredients for precision studies of nuclear spin-dependent parity violation and Schiff moments [35,45].

II. LEVEL STRUCTURE OF THE BAF MOLECULE

The level structure of even isotopologues of BaF, which feature only the nuclear spin of the fluorine atom $I^{(F)} = 1/2$, is similar to that of other alkaline-earth monofluorides used in laser cooling experiments [24] and has been described in detail in previous work [26,42].

In contrast to this, the odd isotopologues, including both ^{135}BaF and ^{137}BaF, which will be studied in detail in this paper, feature two nuclear spins and thus exhibit a complex hyperfine structure. A summary of the level structure of the lowest rotational levels in the $X^2\Sigma^+$ state and the $A^2\Pi_{1/2}$ state is given in Fig. 1. The full Hamiltonian and matrix elements describing these states are summarized in Appendices B and C.

In short, in both ^{137}BaF and ^{135}BaF, the angular momentum structure of the odd isotopologues is shaped by the nuclear spin $I^{(\mathrm{Ba})} = 3/2$ of the respective barium nuclei. The ground state $X^2\Sigma^+$ is described by Hund's case ($b_{\beta S}$) [42], where the electron spin $\mathbf{S}$ strongly couples with the barium nuclear spin $\mathbf{I}^{(\mathrm{Ba})}$ instead of the rotational angular momentum $\mathbf{N}$, reflected in the molecular constants $b_F \gg N \times \gamma$. Here b_F and γ describe the Fermi contact interaction and the coupling strength between electron spin and rotation, respectively, and N is the rotational quantum number associated with $\mathbf{N}$. This coupling leads to an intermediate angular momentum $\mathbf{G} = \mathbf{S} + \mathbf{I}^{(\mathrm{Ba})}$ creating two well-separated manifolds for each rotational level, characterized by the quantum numbers $G = 1$ and $G = 2$. These G manifolds are split by energies comparable to rotations and interact with these rotations $\mathbf{N}$ to produce another intermediate angular momentum $\mathbf{F}_1 = \mathbf{N} + \mathbf{G}$. The fluorine nuclear spin contributes a second, weaker hyperfine interaction. This weak coupling between $\mathbf{F}_1$ and $\mathbf{I}^{(\mathrm{F})}$ is described by the total angular momentum $\mathbf{F} = \mathbf{F}_1 + \mathbf{I}^{(\mathrm{F})}$. These interactions collectively produce a dense hyperfine level structure, as shown in Fig. 1.

The excited state $A^2\Pi_{1/2}$ is described by Hund's case ($a_{\beta J}$) [42]. Here the levels of the rotational ladder, originating from the total angular momentum $\mathbf{J}$ without nuclear spins, split into Λ doublets J^P with opposite well-defined parity $P = \pm$. These states couple to $\mathbf{I}^{(\mathrm{Ba})}$, forming an intermediate angular momentum $\mathbf{F}_1$. Subsequently, $\mathbf{F}_1$ interacts with $\mathbf{I}^{(\mathrm{F})}$, resulting in the total angular momentum $\mathbf{F} = \mathbf{F}_1 + \mathbf{I}^{(\mathrm{F})}$. The magnetic hyperfine interaction for the $A^2\Pi_{1/2}$ state is expressed with the spectroscopic constants d and $h_{1/2} = a - b_F/2 - c/3$, where d corresponds to an off-diagonal correction dominated by the Λ doubling, and a and c describe the magnetic dipole coupling of the nuclear magnetic moment to spin and orbital momentum of the electron. Additionally, the electrostatic hyperfine interaction between the nuclear quadrupole moment and the electric field gradient is reflected in the electric quadrupole parameter eq_0Q. Although hyperfine splitting due to $\mathbf{I}^{(\mathrm{F})}$ is relatively weak in the excited state, it has recently

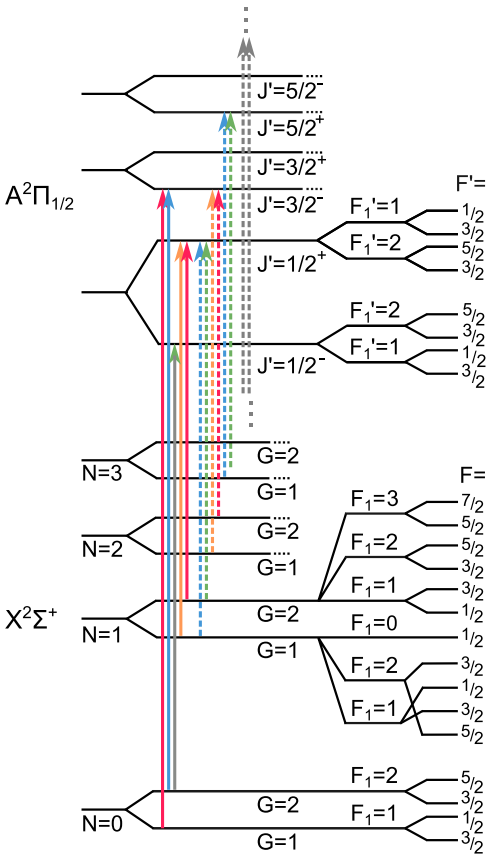

FIG. 1. Level structure of the $X^2\Sigma^+(v) \rightarrow A^2\Pi_{1/2}(v')$ transition in the odd isotopologues of BaF. Here N denotes the rotational, J the total angular momentum without nuclear spins, and G, F_1, and F additional intermediate and hyperfine angular momentum quantum numbers described in the text. Solid arrows indicate transitions probed by fluorescence spectroscopy, which resolves the full hyperfine structure, as shown in Fig. 2. Dashed arrows indicate transitions investigated via absorption spectroscopy, as shown in Fig. 3, with the dash-dotted arrows summarizing any higher transitions probed. Absorption spectroscopy is performed for transitions between different vibrational quantum numbers v and v', which are of important interest as vibrational repumpers in laser cooling. Dots indicate substructures not shown, energy spacings are not to scale, and colors are used for visual clarity. A version of this figure containing all energy spacings extracted in this work can be found in Fig. 9 in Appendix D.

been shown to be resolved in the even isotopologues [26,46], while the hyperfine structure due to $\mathbf{I}^{(\mathrm{Ba})}$ remains largely unexplored, in particular for excited states.

III. FLUORESCENCE SPECTROSCOPY

To explore this hyperfine structure, we perform laser-induced fluorescence spectroscopy on a cryogenic buffer gas-cooled molecular beam [27,47–49] of BaF. We use a neon buffer gas at a temperature of 15 K. Following laser ablation of a Ba metal target in the buffer gas cell, BaF molecules are formed via chemical reaction with a small admixture of SF_6 to the buffer gas. The source is operated at a repetition rate of 10 Hz and produces beams with a mean forward velocity of 180 m/s. Expansion of the buffer gas at the source exit cools the molecules to a rotational temperature of approximately 4 K.

Spectroscopy is carried out approximately 60 cm downstream from the source, where a frequency-tunable laser beam with a wavelength of around 860 nm—stabilized via a transfer cavity lock referenced to a stabilized HeNe laser [50,51]—intersects the molecular beam orthogonally. We calibrate the nonlinearity of the piezo scan of the transfer cavity using a second laser beam, offset by a known radio-frequency interval relative to the primary beam using an acousto-optic modulator. This yields an uncertainty in the relative laser frequency, within a single frequency scan, of 0.3 MHz. The frequency separation between different scans is known to ±100 MHz, from a commercial wavemeter. Molecular fluorescence at the same wavelength as the excitation light is collected in a photomultiplier using mirrors and a light pipe [52,53], and the resulting signals are recorded using standard photon-counting methods.

From prior studies [42,43,54] and the absorption spectroscopy and theory calculations reported below, the electronic and rotational energies, isotope shifts, and ground-state hyperfine structure were sufficiently well known to determine the ground-state quantum numbers N and G, and excited state quantum numbers J'^P, for each of the transitions observed. Specifically, our analysis covered several groups of transitions within the $X(N=0) \rightarrow A(J'^P = 1/2^-)$, $X(N=0) \rightarrow A(J'^P = 3/2^-)$, and $X(N=1) \rightarrow A(J'^P = 1/2^+)$ manifolds. Example results are summarized in Fig. 2. Each spectrum spanned a laser frequency range of 350–400 MHz, which was scanned in steps of 1 MHz. During this procedure the laser frequency was alternately ramped up or down to average over effects of drift or hysteresis. Each of the transitions observed was carefully assigned and fitted, as detailed in Appendix D. We note that in an earlier paper that analyzed the rotational and hyperfine structure of the $A^2\Pi_{1/2}$ state in ^{137}BaF, and ^{135}BaF [42], only higher-lying rotational levels were analyzed, and the Hamiltonian employed there did not include the quadrupole contribution, the contributions with coefficient $h_{1/2}$ for either Ba or F, or the contributions with coefficient d for F. In our analysis of the hyperfine structure, the values of $d^{(F)}$ and $h_{1/2}^{(F)}$ were fixed to those determined in a recent study of the structure of the $A^2\Pi_{1/2}$ levels in ^{138}BaF [46], and the corresponding values $d^{(Ba)}$ and $h_{1/2}^{(Ba)}$ were determined for the two different odd isotopologues ^{135}BaF and ^{137}BaF. The values and associated uncertainties determined for the parameters describing the $A^2\Pi_{1/2}$ hyperfine structure are summarized in Table I.

Since the fits were performed independently for the two isotopologues, it is useful to check the consistency of the extracted molecular parameters against the expected scaling of the intrinsic nuclear parameters, specifically the nuclear magnetic moments (for d and $h_{1/2}$) and nuclear electric quadrupole moments (for eq_0Q). Both types of moments are known for both isotopes from prior atomic spectroscopic measurements [55,56]. Table II presents this comparison, showing excellent agreement.

IV. *AB INITIO* CALCULATIONS OF THE ODD ISOTOPOLOGUE HYPERFINE STRUCTURE

Our measurements provide precise experimental data that can serve as a benchmark for *ab initio* electronic structure calculations of the molecular hyperfine structure. Accurate calculations of this kind require a careful treatment of relativistic and electron-correlation effects, which are also essential for accurately modeling a wide range of molecular properties for precision measurements [57–60].

In particular, the hyperfine structure constants of the excited $A^2\Pi_{1/2}$ state of any odd BaF isotoplogues have not been addressed previously. We thus calculate the parallel and perpendicular components $A_\parallel$ and $A_\perp$ of the hyperfine interaction tensor for the $A^2\Pi_{1/2}$ excited state of ^{137}BaF, using the relativistic four-component Dirac-Coulomb Hamiltonian combined with the Fock-space coupled cluster method and the finite-field approach. Theoretical predictions of the quadrupole constant require a separate and very different computational investigation and will be presented in future work. The calculated hyperfine interaction tensor is related to the molecular constants by $A_\parallel = 2\,h_{1/2}$ and $A_\perp = d$ [46].

In our calculations, we use the DIRAC19 package [61,62]. We correlate all electrons and extrapolate our results to the complete basis set limit, using the dyall.v*n*z basis sets [63–65]. We evaluate the effect of the basis set and electron correlation and estimate the uncertainty on our final values of ∼5% for the $A^2\Pi_{1/2}$ excited state. More details of our calculations and uncertainty estimations, including results for the $A^2\Pi_{3/2}$ state, are summarized in Ref. [66].

Our final results are presented in Table I and show excellent agreement with the experimental data. In most of our previous studies, we found that the method used to estimate uncertainties in the calculated molecular parameters tended to produce error bars that were too conservative, that is, the agreement between theoretical predictions and experimental results was consistently better than anticipated [67,68]. This is not the case in the present work, where the experimental value lies within the theoretical uncertainty for $h_{1/2}$, and slightly outside it (by 0.29 σ) for d. In both cases, the theoretical values are lower than the experimental ones. A similar pattern—where the calculated values and associated uncertainties slightly underestimated the experimental results—was also observed in our previous study of the ^{19}F hyperfine structure contributions in the excited states of ^{138}BaF.

Several effects could be responsible for this pattern. The present study does not account for the Breit interaction or

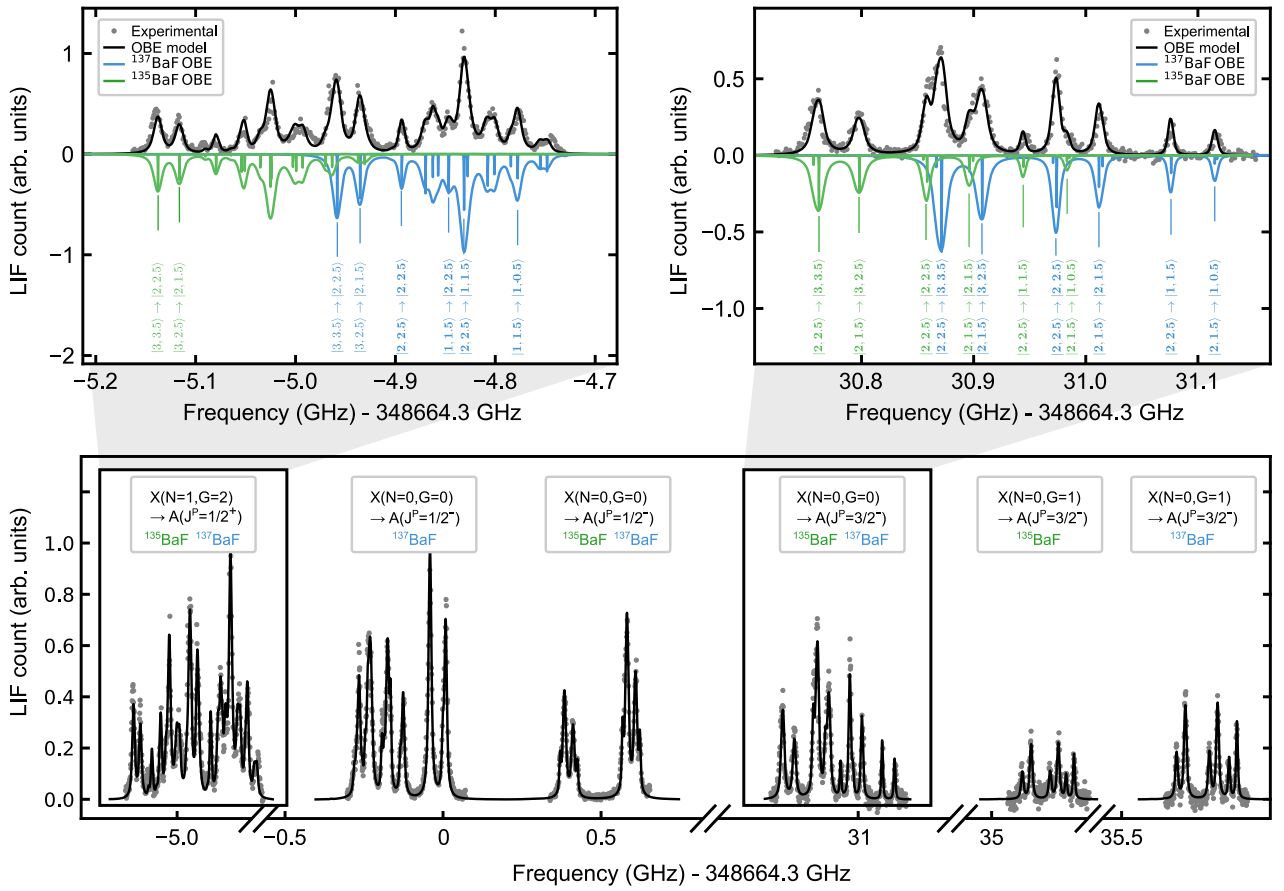

FIG. 2. Fluorescence spectroscopy. Experimental (gray points) and modeled (black curve) spectra spanning all measured transitions arising from different N and G levels in the ^{137}BaF and ^{135}BaF $X^2\Sigma^+$ ground states, and J^P levels in the $A^2\Pi_{1/2}$ states. Each experimental data point in a spectrum scan is typically averaged over 10 repetitions, each taken at a different spots on the ablation target to minimize drifts in molecular signal. With ≈100 μW of incident laser light, signal strengths of 100–1400 counts/pulse are observed, on a background of about 280/pulse from scattered laser light. Backgrounds from scattered laser light are determined from signals outside the time window of the molecular pulse and subtracted. The insets show zoomed-in example scans of the $X(N=1, G=2) \rightarrow A(J^p = 1/2^+)$ and $X(N=0, G=2) \rightarrow A(J^p = 3/2^-)$ transitions, the former being one of the transitions relevant for laser cooling [33]. These plots also show two types of simulated spectra. The first is a "stick plot," showing narrow lines with heights set by the square of the associated transition dipole matrix element. The second is a complete model of the expected spectrum that uses the optical Bloch equations to determine the height and power-broadened width of each line (see Appendix D for details). In the simulated spectra, relative line heights are scaled by the natural abundance of the respective isotopologue, and line positions and dipole matrix elements are set by the final parameters determined in this work. Hyperfine Hamiltonian parameters were determined, for each isotope separately, from splittings between pairs of lines within each continuous spectrum. Separations between the hyperfine centers of gravity for the two isotopes within each continuous spectrum, as well as separations between the disconnected black traces, were varied to minimize the overall goodness of fit. The resulting separations were consistent, within uncertainties, with expectations based on nonhyperfine parameters extracted from the absorption spectroscopy reported in Fig. 3.

QED effects. However, these contributions were found to be negligible for the ground-state hyperfine parameters of ^{137}BaF [68] and are expected to be even smaller in the excited states.

TABLE I. Values of the magnetic hyperfine and electric quadrupole parameters extracted in the current study, all expressed in megahertz (MHz).

Parameter	^{137}BaF Theory	^{137}BaF Experiment	^{135}BaF Experiment
$d^{(\mathrm{Ba})}$	239.1 ± 11.8	254.3 ± 0.5	227.7 ± 1.2
$h^{(\mathrm{Ba})}_{1/2}$	199.5 ± 10.2	206.6 ± 0.3	185.9 ± 0.8
$eq_0Q^{(\mathrm{Ba})}$	–	−89.0 ± 0.7	−56.0 ± 3.1

Additional sources of uncertainty likely stem from the limited model space in the Fock-space coupled-cluster approach and the incompleteness of the employed basis sets. The latter

TABLE II. Comparison of ratios of extracted magnetic dipole (electric quadrupole) hyperfine parameters with the ratios of nuclear magnetic dipole (electric quadrupole) moments of the two isotopes ^{135}Ba and ^{137}Ba [55,56].

Ref. [55]	This work		Ref. [56]	This work
$\frac{\mu^{(137)}}{\mu^{(135)}}$	$\frac{d^{(137)}}{d^{(135)}}$	$\frac{h^{(137)}}{h^{(135)}}$	$\frac{Q^{(137)}}{Q^{(135)}}$	$\frac{eq_0Q^{(137)}}{eq_0Q^{(135)}}$
1.118(5)	1.12(1)	1.11(1)	1.53(4)	1.59(11)

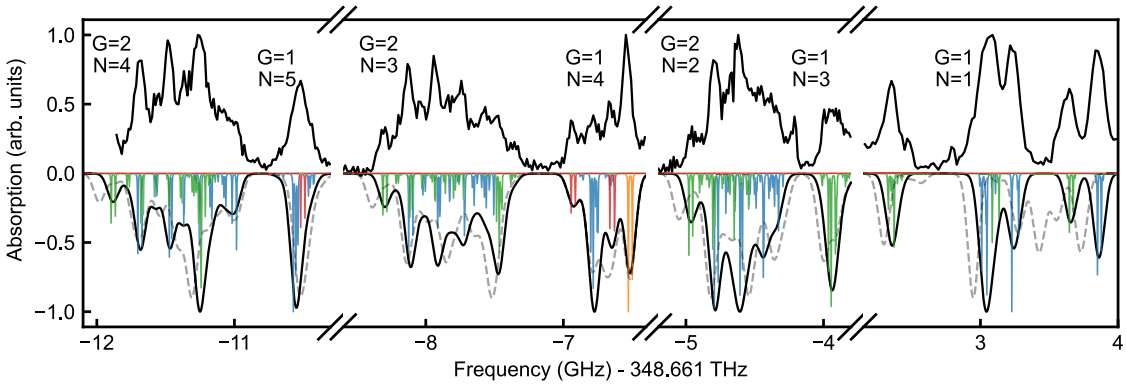

FIG. 3. Example of absorption spectroscopy of BaF. The lines shown belong to the $X(v=0) \rightarrow A(v'=0)$ transition, which is the main cooling transition for laser cooling. Experimental data are shown in the top half of the plot, a prediction based on the constants determined in this work in the bottom half. Labels denote the respective ground-state angular momenta G and N involved in the transitions. Example transitions for $N = 1, 2, 3, \ldots$ and $G = 1, 2$ are indicated in Fig. 1. Individual predicted lines for ^{137}BaF through ^{134}BaF are shown in blue, orange, green, and red, respectively. The envelope shown as a solid black line takes into account the Doppler broadening at 3.5 K, using the molecular constants determined in this work. The dashed line is based on the previous best set of constants [42], which predict significantly shifted transitions and even transitions that were not observed. This discrepancy makes accurate line assignments challenging, underscoring the importance of our fluorescence spectroscopy and theoretical results for reliable assignments. For clarity, the amplitude of the data in every x-axis subsegment has been individually normalized. Residual differences in amplitude between experiment and prediction are due to collisional and optical pumping effects inside the buffer gas source, which will be discussed in future work.

has been shown to be particularly significant in calculations involving excited states [46]. A more detailed discussion of these missing contributions is provided in Ref. [66].

Overall, our results demonstrate that state-of-the-art relativistic electronic structure methods can yield accurate and reliable predictions of hyperfine structure parameters in excited states of small heavy molecules, a domain that had previously remained largely unexplored computationally.

V. ABSORPTION SPECTROSCOPY

After addressing the previously missing information on the hyperfine structure of ^{137}BaF and ^{135}BaF, we now explore the combined absorption spectra of all isotopologues from ^{134}BaF to ^{138}BaF to gain a deeper understanding of the isotope shifts in their rovibrational level structure.

To do so, we use a complementary experimental setup, previously used for the spectroscopic analysis [26,27] and laser cooling [29,32] of the most abundant isotopologues ^{138}BaF and ^{136}BaF. In short, in this setup we create the molecules using laser ablation of a solid BaF_2 precursor in a cryogenic helium buffer gas source at a temperature of $T = 3.5$ K and subsequently record the in-cell absorption. The probing light is derived from a tunable diode laser, and the intensity of the probing beam is stabilized to around 300 μW using an electro-optical amplitude modulator to increase the sensitivity to small changes in absorption. Scanning the laser over a range of 20 + GHz for various transitions produces spectra containing lines from all naturally occurring isotopologes. The typical linewidths observed are around 70 MHz, as given by Doppler, collisional, and residual power broadening in the buffer gas cell. During frequency scans, the probe laser frequency is referenced to wavelength meters that are regularly validated against atomic absorption lines in the same wavelength range. With this, the uncertainty in the absolute frequency calibration is on the order of 50 MHz [26,69].

The high signal-to-noise ratio inside the buffer gas cell allows us to study a large variety of transitions connecting different vibrational levels. Example spectra for the $X^2\Sigma^+(v = 0)$ to $A^2\Pi_{1/2}(v' = 0)$ transition, where v and v' denote the vibrational quantum numbers of the states, are shown in Fig. 3. Building on the precise knowledge of the hyperfine structure obtained in the previous sections, along with the well-established transitions of the more abundant even isotopologues [26], we are able to identify transitions of ^{134}BaF, despite its low natural abundance of only 2.4 %. Moreover, using the hyperfine constants determined above, as well as mass scalings where required, we also find excellent agreement for the transition manifolds of the odd isotopologues ^{135}BaF, and ^{137}BaF.

We use this dataset, as well as similar datasets for transitions between all possible combinations of $v = 0, 1$ and $v' = 0, 1$ to determine the respective absolute energy offsets $T_{v',v} = T'_v - T_v$ of the vibrational states for the various isotopologues. We note that the corresponding transitions are highly relevant in the context of laser cooling, as they are used as repumpers for vibrational leaks. Using the relation $T_v = T_e + \omega_e(v + 1/2) - \omega_e\chi_e(v + 1/2)^2 + \omega_e y_e(v + 1/2)^3$, we fit the values of T_e, ω'_e and ω_e, and summarize the resulting molecular constants for ^{137}BaF, ^{135}BaF, and ^{134}BaF in Table III.

VI. KING PLOT ANALYSIS

In atoms, frequency shifts such as the ones observed are well known to depend both on the center-of-mass changes when transitioning from one isotope to another—the so-called mass shift—and on the overlap of the electronic wave function with the changing nucleus—the so-called field shift. These shifts can be calculated using electronic structure methods. However, such calculations can be challenging, especially for mass shifts and systems with many open-shell electrons.

TABLE III. Molecular constants in units of cm^{-1} for $^{137}Ba\,^{19}F$, $^{135}Ba\,^{19}F$ and $^{134}Ba\,^{19}F$. For unknown values, mass scalings were applied [85,86].

Parameter	$^{137}Ba\,^{19}F$	$^{135}Ba\,^{19}F$	$^{134}Ba\,^{19}F$
$X^2\Sigma^+$			
ω_e	469.6128(17)[e]	470.0381(17)[e]	470.2545(17)[e]
$\omega_e\chi_e$	1.8362[b]	1.8396[c]	1.8413[b]
$10^3\,\omega_e y_e$	3.0666[b]	3.0749[c]	3.0792[b]
$10^3\,B_e$	216.7210[a]	217.1126[a]	217.3130[b]
$10^7\,D_e$	1.8462[a]	1.8529[a]	1.8563[b]
$10^3\,\alpha_e$	1.1651[a]	1.1683[a]	1.1699[b]
$10^3\,\gamma$	2.7014[a]	2.7063[a]	2.7088[b]
$10^3\,b_F$ (F)	2.1965[a]	2.1965[a]	2.1965[b]
$10^3\,c$ (F)	0.2437[a]	0.2437[a]	0.2436[b]
$10^3\,b_F$ (Ba)	77.6681[a]	69.4887[a]	
$10^3\,c$ (Ba)	2.5083[a]	2.2441[a]	
$10^3\,eq_0Q$ (Ba)	−4.7927[a]	−3.1156[a]	
$A^2\Pi$			
T_e	11 962.0587(25)[e]	11 962.0604(25)[e]	11 962.0578(25)[e]
ω_e	438.1472(17)[e]	438.5442(17)[e]	438.7464(17)[e]
$\omega_e\chi_e$	1.8731[b]	1.8765[c]	1.8782[b]
$10^3\,B_e$	212.4585[b]	212.8423[c]	213.0388[b]
$10^7\,D_e$	2.0035[b]	2.0108[c]	2.0145[b]
$10^3\,\alpha_e$	1.1255[b]	1.1286[c]	1.1301[b]
A_e	632.5369[b]	632.5369[c]	632.5369[b]
α_A	−0.5105[b]	−0.5109[c]	−0.5112[b]
$10^3\,A_D$	0.0310[b]	0.0311[c]	0.0311[b]
$p+2q$	−0.2578[b]	−0.2582[c]	−0.2585[b]
$10^3\,a$ (F)	0.8856[b]	0.8856[c]	0.8856[b]
$10^3\,b_F$ (F)	−0.0667[b]	−0.0667[c]	−0.0667[b]
$10^3\,c$ (F)	−0.1771[b]	−0.1771[c]	−0.1771[b]
$10^3\,d$ (F)	0.1194[b]	0.1194[c]	0.1194[b]
$10^3\,h_{1/2}$ (Ba)	6.8948(133)[d]	6.1976(200)[d]	
$10^3\,d$ (Ba)	8.4825(167)[d]	7.5953(367)[d]	
$10^3\,eq_0Q$ (Ba)	−2.9721(467)[d]	−1.8680(901)[d]	

[a]Reference [43].
[b]Value obtained from scaling the value for $^{138}Ba\,^{19}F$ [26].
[c]Value obtained from scaling the value for $^{137}Ba\,^{19}F$.
[d]Value obtained from fluorescence spectroscopy fit.
[e]Value obtained from absorption spectroscopy fit.

A well established tool to circumvent this problem for atomic isotope shifts are King plots, where the shifts of two transitions are compared relative to each other, which removes the need for precise knowledge of the nuclear charge radius, and for accurate theoretical predictions of the field and the mass shifts [71]. This results, to first order, in a linear plot, where the slope and the vertical intercept are directly related to the mass and field shift parameters. We note briefly that deviations from this linearity at much higher levels of precision have recently gained interest as probes of physics beyond the standard model [72–74].

As in atoms, it has recently been shown that isotope shifts in molecules can also be expressed as the sum of a field shift and a mass shift [14]. Several observations of field shifts in molecular spectra have also been previously reported [75–77]. Building on this, our experimental results enable a comprehensive analysis of isotope shifts in BaF molecules, offering two key benefits.

First, the linearity of a King plot provides an additional, robust way to validate line assignments in the observed rovibrational spectra, since an incorrect assignment would immediately stand out in the King plot. This is particularly useful for the analysis of molecular beams containing many different, potentially rare or short-lived isotopologues.

Second, the argument can be turned around and the King plot can be used to extract information about the nuclear charge radius, and thus about nuclear structure. Similar high-precision atomic spectroscopy of isotope shifts has long been a key tool for studying nuclear structure using laser spectroscopy, providing important benchmarks for nuclear theory. As we demonstrate in the following, similar information can be obtained from molecular spectroscopy, which is particularly attractive for short-lived nuclei created in online facilities, where the formation of molecules, rather than atoms, is often unavoidable [14,78,79].

The results of our analysis are summarized in Fig. 4. For the King plots, we compare isotope shifts of transitions between different molecular vibrational levels with each other, as encoded by the respective offsets $T_{v,v'}$. This results in a King plot derived entirely from molecular data, where, unlike in most atomic systems, lasers with vastly different wavelengths are not necessarily required. In addition, we compare the transitions individually with known barium atomic spectroscopy, as previously established in [14]. The linearity of the results validates our assignments of the molecular transitions for all isotopologues [70]. Moreover, using the knowledge of existing mass and field shift constants, we also extract the relative change in the nuclear charge radius of the barium nuclei [70]. In this process, we probe nuclei containing 56 protons, and a varying number of neutrons from 78 for ^{134}BaF, to 82 for ^{138}BaF.

The resulting nuclear charge radii typically scale as $A^{1/3}$ with the total number of nucleons A in simple nuclear models [80]. However, in addition to this well-known increase in size for an increasing number of nucleons, we observe that isotopes with an odd number of neutrons are reduced in size compared to even neutron isotopes. In other words, the addition of an extra neutron can, counterintuitively, make the nucleus smaller rather than larger. This odd-even staggering effect arises from nontrivial many-body effects in the nucleus, which form a formidable challenge for nuclear *ab initio* calculations [81–83]. Our example results highlight that high-resolution molecular spectroscopy, combined with King plot analysis, can provide access to nuclear charge radii, offering a promising approach in cases where molecular spectra are more accessible or experimentally favorable than atomic spectra [77]. Considering recent progress in molecular spectroscopy, for example, with regard to molecular clocks [13,84], it is conceivable that molecules could thus contribute significantly to future measurements of nuclear charge radii and nuclear structure in general.

VII. CONCLUSION

We have presented a comprehensive investigation of the energy level structure of most stable isotopologues of the BaF molecule.

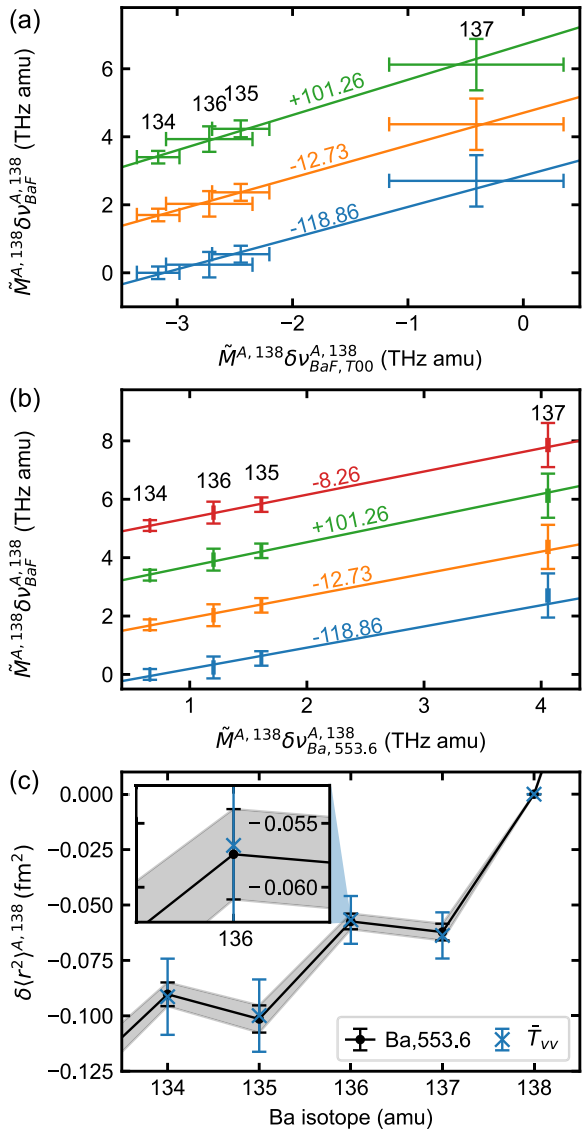

FIG. 4. King plot analysis and odd-even staggering of the barium nuclear charge radius. (a) Isotope shifts of BaF's (from top to bottom) T_{01} (green), T_{11} (orange) and T_{10} (blue) constants relative to the T_{00} constant. (b) Isotope shifts of T_{00} (red), as well as the transitions above, compared to the 553.6 nm transition in atomic barium [70]. Lines in (a) and (b) have been vertically offset for visual clarity, with their offset values indicated. (c) Relative change in nuclear charge radius $\delta\langle r^2\rangle$, as determined by combining our data with previously known mass and field shift values [14]. Data points are averaged over all molecular transitions studied in (a) and (b), and are in excellent agreement with atomic reference data (solid line). Error bars of the atomic data (shaded area) are derived from uncertainties in the atomic isotope, mass and field shifts [70], and the inset highlights the agreement at the 1%–2% level.

Our detailed comparison of *ab initio* calculations of the excited state hyperfine structure with experiments provides an important benchmark for the former in a so far little explored regime. This, in turn, strengthens similar calculations that directly support the extraction of standard model parameters from experiments [60].

Moreover, the spectroscopic results presented here are an important step towards achieving or improving laser cooling and cycling detection for odd, and by extrapolation, short-lived isotopologues of BaF. While the rovibronic transitions studied provide the necessary frequencies for repumping vibrational losses, the analysis of the excited-state hyperfine structure provides input for the optimization of the cooling forces through engineering of laser sidebands [29,87]. Knowledge about this hyperfine structure also allows us to estimate the expected degree of hyperfine mixing in the excited state, which is known to disrupt rotational selection rules in molecules such as YbOH [88]. In the even isotopologues of BaF, the states $J = 1/2^+, F = 1$ and $J = 3/2^+, F = 1$ are mixed via a lambda-doubling-type hyperfine interaction, specifically the $d^{(F)}$ term. In contrast, the odd isotopologues exhibit a greater number of mixed levels due to increased hyperfine interactions from the $d^{(Ba)}$ term, resulting in a more significant and problematic loss mechanism. Although our results indicate slightly less favorable branching ratios than previously assumed [42,44], they show that ^{137}BaF, and ^{135}BaF, can scatter at least on the order of 2000 photons, before branching into the typically unaddressed $N = 3$ rotational level occurs. This loss rate is comparable to the one known to occur in BaF through the intermediate electronic Δ state, which, in contrast, leads to decays to rotational levels $N = 0$ and $N = 2$ with opposite parity. Losses to all these rotational levels have recently been addressed in the realization of a magneto-optical trap for ^{138}BaF [31]. We therefore anticipate that similar repumping schemes can be used to realize a magneto-optical trap for odd BaF isotopologues without a significant increase in experimental complexity.

Finally, the precise knowledge of the isotope shifts along a chain of isotopologues provides input to a King plot analysis that reveals the odd-even staggering of the nuclear charge radius of the barium atom. The precision of this approach could be significantly improved in the future using improved molecular spectroscopy techniques [89] or molecular clocks [13,84] to make it competitive with atomic spectroscopy, where many open questions remain [90]. As a similar level of spectroscopic resolution has already been demonstrated with radioactive molecular species, this opens up new approaches for the study of short-lived nuclei, including their higher-order nuclear moments, which provide important enhancements in sensitivity for precision measurements of fundamental nuclear properties [37].

ACKNOWLEDGMENTS

We thank Andreas Schindewolf, Timothy Steimle, Richard Mawhorter, and Edward Grant for fruitful discussions. D.D. and M.B. thank Sidney B. Cahn for extensive contributions to the fluorescence spectroscopy apparatus. T.L., F.K., M.R., and T.G. acknowledge Tilman Pfau for generous support, as well as Ralf Albrecht and Einius Pultinevicius for contributions in the early stage of the experiment. The fluorescence spectroscopy work was supported by Laboratory Directed Research and Development (LDRD) funding from Argonne National Laboratory, provided by the Director, Office of Science, of the U.S. DOE under Contract No. DEAC02-06CH11357. A.B. and Y.C. thank the Center for

Information Technology at the University of Groningen for their support and for providing access to the Peregrine and Hábrók high-performance computing clusters, and acknowledge the support from the Dutch Research Council, NWM (VI.Vidi.192.088). The absorption spectroscopy work has received funding from the European Research Council (ERC) under the European Union's Horizon 2020 research and innovation programme (Grant Agreement No. 949431), the RiSC program of the Ministry of Science, Research and Arts Baden-Württemberg, and the Carl Zeiss Foundation, and was funded in whole or in part by the Austrian Science Fund (FWF) 10.55776/PAT8306623.

DATA AVAILABILITY

The data that support the findings of this article are not publicly available. The data are available from the authors upon reasonable request.

APPENDIX A: KING PLOT ANALYSIS PROCEDURE

We summarize here the procedure used to extract from the King plot analysis [14,91].

1. King plots for atoms

In atomic systems, frequency shifts between the same transitions of two isotopes A and A' are well understood to arise from two primary effects: the mass shift, which originates from changes in the center-of-mass motion, and the field shift, which results from variations in the nucleus' electromagnetic field seen by core-penetrating electrons. While the former is proportional to the relative difference

$$\frac{1}{\tilde{M}^{A',A}} = \frac{M_{A'} - M_A}{M_{A'} M_A} \tag{A1}$$

of the atomic masses $M_{A'}$ and M_A, the latter contribution depends on the nuclear charge radius $\delta\langle r^2\rangle^{A,A'}$. Taken together, the isotope shift of a certain transition i can be expressed as a sum of both contributions with the F and K being the field-shift and mass-shift factors, respectively:

$$\delta\nu_i^{A,A'} = F_i\,\delta\langle r^2\rangle^{A,A'} + K_i\,\frac{1}{\tilde{M}^{A',A}}. \tag{A2}$$

By comparing the shifts of two different transitions i and j, a King plot analysis allows for calculating the nuclear charge radius [71] when combining and rearranging the equation to

$$\tilde{M}^{A',A}\,\delta\nu_i^{A,A'} = \frac{F_i}{F_j}\,\tilde{M}^{A',A}\,\delta\nu_j^{A,A'} + \left(K_i - \frac{F_i}{F_j}K_j\right). \tag{A3}$$

To first order, the resulting plot is linear, with the slope and intercept directly linked to the mass and field shift parameters.

2. Nuclear charge radius from molecular transitions

Recent work has extended this concept to molecular systems, demonstrating that isotope shifts in molecules can also be described as the sum of mass and field shifts in Eq. (A2) [14]. This insight enables a comprehensive analysis of the isotope shifts observed in BaF, based on our experimental results.

By plotting the isotope shifts of the isotopologues ^{134}BaF, ^{135}BaF, ^{136}BaF, and ^{137}BaF against the transition T_{00} of ^{138}BaF as a reference for the molecular transitions T_{01}, T_{11}, and T_{10}, reveals the expected linear behavior in Eq. (A3) for purely molecular king plots in Fig. 4(a). Next, all aforementioned transitions $T_{v,v'}$ are compared with atomic data for the 553.6 nm transition known from barium spectroscopy [70], as described in [14]. The data points in Fig. 4(b) also showing a perfectly linear behavior confirm our extracted molecular constants for all isotopologues.

In addition, utilizing established field and mass shift constants, $F_{553.6\,\mathrm{nm}} = (-4.48 \pm 0.26)\,\frac{\mathrm{GHz}}{\mathrm{fm}^2}$ and $M_{553.6\,\mathrm{nm}} = (1207 \pm 186)\,\mathrm{GHz}$, along with the slope and y axis offsets according to Eq. (A3), the relative change in the nuclear charge radius of the barium nuclei with respect to ^{138}BaF can be determined [70]. Here the error bars of the atomic data (shaded area) are determined from respective uncertainties in the atomic isotope, mass and field shifts. This analysis allows for the exploration of a nuclei containing 56 protons, and a varying number of neutrons from 78 in ^{134}BaF to 82 in ^{138}BaF.

APPENDIX B: DESCRIPTION OF THE MOLECULAR HYPERFINE INTERACTION

In the following, we present the effective Hamiltonian employed to describe the rotational and hyperfine structure of the odd isotopologues of BaF. We start by introducing the appropriate basis states for the individual electronic levels to be studied.

1. Basis states

a. $X^2\Sigma^+$ *state*

The $X^2\Sigma^+$ states of ^{137}BaF and ^{135}BaF are best described in the Hund's case (b) basis. Here the effective rotational angular momentum $\mathbf{N}$ is given by $\mathbf{N} = \mathbf{R} + \mathbf{L}$, where $\mathbf{R}$ is the pure rotational angular momentum and $\mathbf{L}$ is the electron orbital angular momentum. In subcase ($b_{\beta S}$) the magnetic dipole hyperfine interaction with the Ba nucleus couples the electron spin $\mathbf{S}$ strongly with the nuclear spin $\mathbf{I}^{(\mathrm{Ba})}$ to form the intermediate angular momentum $\mathbf{G} = \mathbf{S} + \mathbf{I}^{(\mathrm{Ba})}$ [42]. Then $\mathbf{G}$ couples with $\mathbf{N}$ to form $\mathbf{F_1} = \mathbf{G} + \mathbf{N}$. This quantity finally couples with the ^{19}F nuclear spin, $\mathbf{I}^{(\mathrm{F})}$, to produce the total angular momentum $\mathbf{F} = \mathbf{F_1} + \mathbf{I}^{(\mathrm{F})}$. We write the basis states for $X^2\Sigma^+$ as

$$|\eta\Lambda; S, I^{(\mathrm{Ba})}, G, N, F_1, I^{(\mathrm{F})}, F, m_F; P\rangle\,,$$

where η represents all nonangular momentum quantum numbers; $\Lambda = 0$ is the projection of $\mathbf{L}$ on the internuclear axis; $S = 1/2$, G, N, F_1, F are the quantum numbers associated with $\mathbf{G}$, $\mathbf{N}$, $\mathbf{F_1}$, and $\mathbf{F}$ respectively, and m_F is the projection of $\mathbf{F}$ on the laboratory Z axis. These states have parity quantum number $P = (-1)^N$.

b. $A^2\Pi_{1/2}$ *state*

The Hund's case (a) basis is a good representation for the sublevels of the $A^2\Pi_{1/2}$ states [42] in BaF. Here $\mathbf{S}$ and $\mathbf{L}$ couple with $\mathbf{R}$ to produce the total angular momentum excluding nuclear spins, $\mathbf{J} = \mathbf{L} + \mathbf{S} + \mathbf{R}$. Next, $\mathbf{I}^{(\mathrm{Ba})}$ couples with $\mathbf{J}$ to

produce an intermediate angular momentum, $\mathbf{F_1} = \mathbf{J} + \mathbf{I}^{(\mathrm{Ba})}$. The coupling of $\mathbf{F_1}$ with $\mathbf{I}^{(\mathrm{F})}$ generates the total angular momentum, $\mathbf{F} = \mathbf{F_1} + \mathbf{I}^{(\mathrm{F})}$. We describe the $A^2\Pi_{1/2}$ states using a basis with quantum numbers $\Lambda = \pm 1$, $\Sigma = \pm 1/2$, (the signed projections of $\mathbf{L}$ and $\mathbf{S}$ on the intermolecular axis, respectively), plus $\Omega \equiv \Lambda + \Sigma = \pm 1/2$, F_1, F, and m_F. Finally, we write the basis states with signed values of Ω as

$$|\psi\rangle_\Omega = |\eta\Lambda, S, \Sigma, J, \Omega; J, I^{(\mathrm{Ba})}, F_1, I^{(\mathrm{F})}, F, m_F\rangle\,. \tag{B1}$$

The energy and parity eigenstates, $|\psi\rangle_\mathrm{P}$, can be written as a superposition of the signed-Ω basis states:

$$|\psi\rangle_\mathrm{P} = \frac{1}{\sqrt{2}}(|\Lambda, S, \Sigma, \Omega; J, I^{(\mathrm{Ba})}, F_1, I^{(\mathrm{F})}, F, m_F\rangle + (-1)^p P\,|-\Lambda, S, -\Sigma, -\Omega; J, I^{(\mathrm{Ba})}, F_1, I^{(\mathrm{F})}, F, m_F\rangle), \tag{B2}$$

where $p = J - S$ and $P = \pm 1$ is the parity of the state. For the $\Pi_{1/2}$ states, $\Lambda = \pm 1$, $\Sigma = \mp 1/2$, and $\Omega = \Lambda + \Sigma = \pm 1/2$.

2. Effective hyperfine/rotation Hamiltonians

Effective Hamiltonians describing hyperfine and rotational motion in a single vibronic level of $^2\Sigma^+$ and $^2\Pi_{1/2}$ states with two nuclear spins have been summarized in Ref. [92]. The effective Hamiltonian for the $X^2\Sigma^+$ state is given by

$$\begin{aligned} H_{^2\Sigma^+} &= B\mathbf{N}^2 - D\mathbf{N}^4 + \gamma\mathbf{N}\cdot\mathbf{S} \\ &\quad + b^{(\mathrm{Ba})}\mathbf{I}^{(\mathrm{Ba})}\cdot\mathbf{S} + c^{(\mathrm{Ba})}\left(I_z^{(\mathrm{Ba})}S_z - \frac{1}{3}\mathbf{I}^{(\mathrm{Ba})}\cdot\mathbf{S}\right) \\ &\quad + eq_0Q^{(\mathrm{Ba})}\frac{3I_z^{(\mathrm{Ba})} - \mathbf{I}^{(\mathrm{Ba})}\cdot\mathbf{I}^{(\mathrm{Ba})}}{4I^{(\mathrm{Ba})}(2I^{(\mathrm{Ba})}-1)} \\ &\quad + b^{(\mathrm{F})}\mathbf{I}^{(\mathrm{F})}\cdot\mathbf{S} + c^{(\mathrm{F})}\left(I_z^{(\mathrm{F})}S_z - \frac{1}{3}\mathbf{I}^{(\mathrm{F})}\cdot\mathbf{S}\right). \end{aligned} \tag{B3}$$

Here B and D parametrize the rotational and the centrifugal distortion corrections energies, and γ describes the strength of the electron spin coupling with molecular rotation. The terms with coefficients $b = b_F - c/3$ and c, indexed by the nucleus in the superscript, represent the Fermi contact interaction and the electron spin-nuclear spin dipolar interaction, respectively. The subscript z refers to the direction along the internuclear axis in the molecule-fixed frame. The nuclear quadrupole moment of the Ba nucleus, $Q^{(\mathrm{Ba})}$, couples to the electric field gradient caused by the valence electron, eq_0, which contributes an electric quadrupole term parametrized by $eq_0Q^{(\mathrm{Ba})}$. The values of these parameters were already established with high accuracy via microwave spectroscopy [43,54], and we treat them as fixed in our analysis.

We write the $^2\Pi_{1/2}$ state Hamiltonian as

$$\begin{aligned} H_{^2\Pi_{1/2}} &= \tfrac{1}{2}A_D\{L_zS_z, \mathbf{R}\} + B\mathbf{R}^2 - D\mathbf{R}^4 \\ &\quad + \tfrac{1}{2}(p+2q)(e^{-2i\phi}J_+S_+ + \mathrm{H.c.}) + H^{\mathrm{HF}}_{\Pi_{1/2}}. \end{aligned} \tag{B4}$$

Here A_D characterizes the centrifugal distortion of the spin-orbit interaction; $\{\}$ denotes the anticommutator; $p+2q$ characterizes the Λ-doubling; the subscripts $\pm$ correspond to spin raising and lowering operators, respectively, in the molecule's body fixed frame, H.c. denotes the Hermitian conjugate of the preceding expression. and $H^{\mathrm{HF}}_{\Pi_{1/2}}$ describes the hyperfine interaction. Values of the parameters A_D, B, D, and $p+2q$ have been measured by Steimle *et al.* [42] and also by absorption spectroscopy in the current work. We fix these parameters to the values determined in the current work for our analysis of the hyperfine structure. Following the form of the Hamiltonian used in Ref. [46] for the magnetic hyperfine terms and Ref. [92] for the quadrupole term, we write the hyperfine Hamiltonian as

$$\begin{aligned} H^{\mathrm{HF}}_{\Pi_{1/2}} &= H^{(\mathrm{F})}_{h_{1/2}} + H^{(\mathrm{F})}_d + H^{(\mathrm{Ba})}_{h_{1/2}} + H^{(\mathrm{Ba})}_d + H^{(\mathrm{Ba})}_{\mathrm{Q}} \\ &= h^{(\mathrm{F})}_{1/2}I^{(\mathrm{F})}_z + \frac{1}{2}d^{(\mathrm{F})}[e^{2i\phi}I^{(\mathrm{F})}_-S_- + e^{-2i\phi}I^{(\mathrm{F})}_+S_+] \\ &\quad + h^{(\mathrm{Ba})}_{1/2}I^{(\mathrm{Ba})}_z + \frac{1}{2}d^{(\mathrm{Ba})}[e^{2i\phi}I^{(\mathrm{Ba})}_-S_- + e^{-2i\phi}I^{(\mathrm{Ba})}_+S_+] \\ &\quad + eq_0Q^{(\mathrm{Ba})}\frac{3I^{(\mathrm{Ba})}_z - \mathbf{I}^{(\mathrm{Ba})}\cdot\mathbf{I}^{(\mathrm{Ba})}}{4I^{(\mathrm{Ba})}(2I^{(\mathrm{Ba})}-1)}. \end{aligned} \tag{B5}$$

The magnetic hyperfine coefficient $h_{1/2}$ can be expressed in terms of the Frosch and Foley a, b, and c parameters [93] as

$$h_{1/2} = a - \frac{1}{2}(b+c) = a - \frac{b_F}{2} - \frac{c}{3}. \tag{B6}$$

Note that both parameters $h^{(\mathrm{Ba})}_{1/2}$ and $d^{(\mathrm{Ba})}$ are proportional to the nuclear magnetic moment of the relevant isotope, $\mu^{(\mathrm{Ba})}$, while the quadrupole term $eq_0Q^{(\mathrm{Ba})}$ is proportional to their electric quadrupole moments $Q^{(\mathrm{Ba})}$.

APPENDIX C: MATRIX ELEMENTS OF THE HYPERFINE HAMILTONIAN FOR THE $A^2\Pi_{1/2}$ STATE

We provide here expressions for the matrix elements of the magnetic hyperfine and nuclear electric quadrupole interaction terms in the Hund's case (a) basis.

a. Matrix elements of $H^{(\mathrm{Ba})}_{h_{1/2}}$

$$\begin{aligned} &\langle\eta\Lambda, S, \Sigma, J, \Omega; J, I_1, F_1, I_2, F, m_F\,|\,H^{(\mathrm{Ba})}_{h_{1/2}}\,|\eta\Lambda', S, \Sigma', J', \Omega'; J', I_1, F_1', I_2, F', m_F'\rangle \\ &= h^{(\mathrm{Ba})}_{1/2}\Lambda\delta_{\Lambda,\Lambda'}(-1)^{J-\Omega}\begin{pmatrix} J & 1 & J' \\ -\Omega & 0 & \Omega'\end{pmatrix}[JJ']^{1/2}\delta_{m_F,m_F'}\delta_{F,F'}\delta_{F_1,F_1'}(-1)^{J'+F_1+I_1}\{I_1\}^{1/2}\begin{Bmatrix} I_1 & J' & F_1 \\ J & I_1 & 1\end{Bmatrix} \end{aligned} \tag{C1}$$

b. Matrix elements of $H^{(\mathrm{F})}_{h_{1/2}}$

$$\begin{aligned}
&\langle \eta\Lambda, S, \Sigma, J, \Omega; J, I_1, F_1, I_2, F, m_F \big| H^{(\mathrm{F})}_{h_{1/2}} \big| \eta\Lambda', S, \Sigma', J', \Omega'; J', I_1, F_1', I_2, F', m_F' \rangle \\
&= h^{(\mathrm{F})}_{1/2} \Lambda \delta_{\Lambda,\Lambda'} (-1)^{J-\Omega} \begin{pmatrix} J & 1 & J' \\ -\Omega & 0 & \Omega' \end{pmatrix} [JJ']^{1/2} \\
&\quad \times \delta_{m_F,m_F'} \delta_{F,F'} \delta_{F_1,F_1'} (-1)^{2F_1'+F+I_2+J+I_1+1} [F_1 F_1']^{1/2} \begin{Bmatrix} I_2 & F_1' & F \\ F_1 & I_2 & 1 \end{Bmatrix} \begin{Bmatrix} J' & F_1' & I_1 \\ F_1 & J & 1 \end{Bmatrix} \{I_2\}^{1/2}
\end{aligned} \tag{C2}$$

c. Matrix elements of $H^{(\mathrm{Ba})}_d$

$$\begin{aligned}
&\langle \eta\Lambda, S, \Sigma, J, \Omega; J, I_1, F_1, I_2, F, m_F \big| H^{(\mathrm{Ba})}_d \big| \eta\Lambda', S, \Sigma', J', \Omega'; J', I_1, F_1', I_2, F', m_F' \rangle \\
&= \left[\delta_{\Lambda,\Lambda'+2} \begin{pmatrix} S & 1 & S \\ -\Sigma & -1 & \Sigma' \end{pmatrix} \begin{pmatrix} J & 1 & J' \\ -\Omega & 1 & \Omega' \end{pmatrix} + \delta_{\Lambda,\Lambda'-2} \begin{pmatrix} S & 1 & S \\ -\Sigma & 1 & \Sigma' \end{pmatrix} \begin{pmatrix} J & 1 & J' \\ -\Omega & -1 & \Omega' \end{pmatrix} \right] \\
&\quad \times d^{(\mathrm{Ba})} (-1)^{S-\Sigma+J-\Omega} [JJ']^{1/2} \{S\}^{1/2} \delta_{m_F,m_F'} \delta_{F,F'} \delta_{F_1,F_1'} (-1)^{J'+F_1+I_1} \begin{Bmatrix} I_1 & J' & F_1 \\ J & I_1 & 1 \end{Bmatrix} \{I_1\}^{1/2}
\end{aligned} \tag{C3}$$

d. Matrix elements of $H^{(\mathrm{F})}_d$

$$\begin{aligned}
&\langle \eta\Lambda, S, \Sigma, J, \Omega; J, I_1, F_1, I_2, F, m_F \big| H^{(\mathrm{F})}_d \big| \eta\Lambda', S, \Sigma', J', \Omega'; J', I_1, F_1', I_2, F', m_F' \rangle \\
&= \left[\delta_{\Lambda,\Lambda'+2} \begin{pmatrix} S & 1 & S \\ -\Sigma & -1 & \Sigma' \end{pmatrix} \begin{pmatrix} J & 1 & J' \\ -\Omega & 1 & \Omega' \end{pmatrix} + \delta_{\Lambda,\Lambda'-2} \begin{pmatrix} S & 1 & S \\ -\Sigma & 1 & \Sigma' \end{pmatrix} \begin{pmatrix} J & 1 & J' \\ -\Omega & -1 & \Omega' \end{pmatrix} \right] \\
&\quad \times d^{(\mathrm{F})} (-1)^{S-\Sigma+J-\Omega} [JJ']^{1/2} \{S\}^{1/2} \delta_{m_F,m_F'} \delta_{F,F'} (-1)^{2F_1'+F+I_2+J+I_1+1} [F_1 F_1']^{1/2} \begin{Bmatrix} I_2 & F_1' & F \\ F_1 & I_2 & 1 \end{Bmatrix} \begin{Bmatrix} J' & F_1' & I_1 \\ F_1 & J & 1 \end{Bmatrix} \{I_2\}^{1/2}
\end{aligned} \tag{C4}$$

e. Matrix element of H_Q

$$\begin{aligned}
&\langle \eta\Lambda, S, \Sigma, J, \Omega; J, I_1, F_1, I_2, F, m_F \big| H_Q \big| \eta\Lambda', S, \Sigma', J', \Omega'; J', I_1, F_1', I_2, F', m_F' \rangle \\
&= \frac{eq_0 Q^{(\mathrm{Ba})}}{4} \delta_{\Sigma,\Sigma'} (-1)^{J-\Omega} \begin{pmatrix} J & 2 & J' \\ -\Omega & 0 & \Omega' \end{pmatrix} [JJ']^{1/2} \delta_{m_F,m_F'} \delta_{F,F'} \delta_{F_1,F_1'} (-1)^{J'+F_1+I_1} \begin{Bmatrix} I_1 & J & F_1 \\ J' & I_1 & 2 \end{Bmatrix} \begin{pmatrix} I_1 & 2 & I_1 \\ -I_1 & 0 & I_1 \end{pmatrix}^{-1}
\end{aligned} \tag{C5}$$

Here we have used the following short hand notations as in Ref. [94]:

$$\{A\} = A(A+1)(2A+1),$$
$$[AB] = (2A+1)(2B+1).$$

From these expressions, it can be seen that the magnetic hyperfine interaction mixes different J states with the selection rule $\Delta J = \pm 1$. Since we find mixing matrix elements as large as ∼100 MHz (based on the parameters extracted in the current work), and with the separation between consecutive J levels of ∼10 GHz, we expect a mixing of order 1% between nearby J states. The quadrupole Hamiltonian, on the other hand, mixes J states with the selection rule $\Delta J = \pm 2$. For our final analysis, we diagonalize the Hamiltonian for the $A^2\Pi_{1/2}$ state by including all basis states with values of J from 1/2 to 7/2, and both parities.

This hyperfine mixing between the states $J' = 1/2^+$ and $J' = 3/2^+$ of $A^2\Pi_{1/2}$ also has important consequences for laser cooling, which relies on selection rules to limit rotational branching. Whereas the pure state $J' = 1/2^+$ only branches into levels of the rotational level $N = 1$ of the ground state $X^2\Sigma^+$, the state $J' = 3/2^+$ decays with similar probabilities into $N = 1$ and $N = 3$. The small mixing of these two J' states therefore creates a leakage of approximately 0.05 % into $N = 3$ that allows the scattering of approximately 2000 photons. We note that this value is of the same order of magnitude as the branching ratio into the intermediate $A'\Delta$ state previously studied in the bosonic isotopologues [27,95].

To recover these molecules, neighboring rotational states are typically mixed by applying microwave radiation [96]. As the number of ground states involved in the optical cycle increases significantly, the maximum scattering rate is substantially reduced. To address this, an alternative approach is to drive optical transitions, specifically, the $X^2\Sigma^+(N = 3)$ to $A^2\Pi_{1/2}(J' = 3/2^+)$ transition in this case [31,97].

APPENDIX D: NUMERICAL MODELING OF THE SPECTRA

Transition dipole matrix elements were computed by diagonalizing the hyperfine and rotational Hamiltonians, transforming X state kets into the Hund's case (a) basis, and applying standard formulas for line strengths between case (a) states. This information was sufficient to produce the "stick plots" in Figs. 5–8.

To reproduce the measured spectra and to make estimates of systematics, we model the light-atom interaction with the optical Bloch equations (OBEs) [98,99]. This approach is

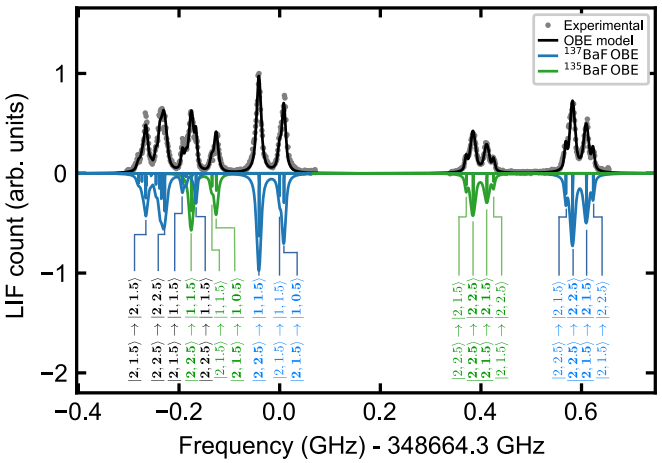

FIG. 5. Experimental (gray dots) and modeled (black curve) spectra for the $X\,|N=0,G=2,F_1,F\rangle \rightarrow A\,|J'^P=1/2^-,F_1',F'\rangle$ transitions in ^{135}BaF and ^{137}BaF (with individual modeled spectra and quantum numbers $|F_1,F\rangle \rightarrow |F_1',F'\rangle$ labeled in green and blue, respectively). Also shown is the $X\,|N=1,G=1,F_1,F\rangle \rightarrow A\,|J'^P=1/2^+,F_1',F'\rangle$ transition in ^{137}BaF (with quantum numbers in blue), which overlaps partially with this frequency range. Among the transitions labeled in the diagram, only the ones in bold were used in the quantitative analysis. A stick plot depicting all transitions, with strength proportional to the square of the transition dipole matrix elements, is overlaid on the full modeled spectrum generated using simulations based on the optical Bloch equations. Note that for the simulated spectra shown here (and in all figures), the center of mass of each isotopologue and rotation state was adjusted to maximize overlap with the data. The resulting adjustments were well within the range of uncertainties for the rotational and isotope splittings determined via absorption spectroscopy.

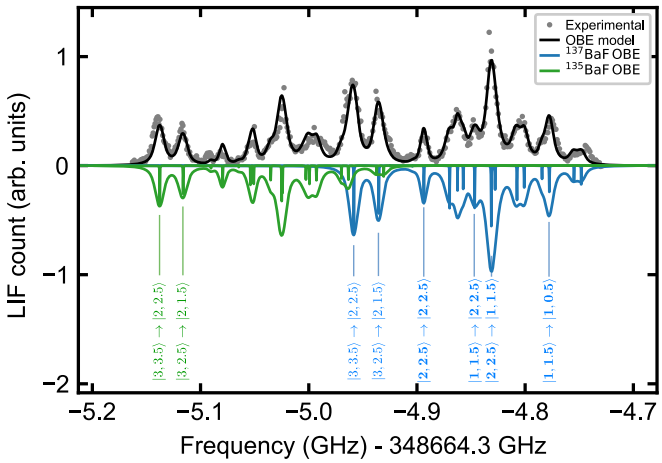

FIG. 6. Spectra for the $X\,|N=1,G=2,F_1,F\rangle \rightarrow A\,|J'^P=1/2^+,F_1',F'\rangle$ transitions in $^{135/137}$BaF. All notations are as in Fig. 5.

required to account for saturation and (partial) optical cycling effects, which affect the relative line strengths and widths. For this, absolute line strengths were computed using the known spontaneous decay rate $\Gamma = 2\pi \times 2.7\,\text{MHz}$ of the $A^2\Pi_{1/2}$ state [100]. We numerically integrate the OBEs taking into account the Gaussian shape of the laser beam and associated spatial and temporal distribution of intensity experienced by the ensemble of molecules in the beam. The effect of the laboratory magnetic field was included to account for remixing of dark states on transitions that could accommodate some optical cycling. We also account for Doppler broadening from the transverse velocity distribution of the molecular ensemble, computed from the known collimation geometry and mean forward velocity of the beam.

Note that similar modeling for the absorption spectroscopy data taken inside a buffer gas cell is challenging. The high rate of collisions inside the buffer gas cell means that the coherences revealed by the OBEs (and associated optical pumping, optical cycling, saturation of signals with laser power, etc.) will be strongly altered. The corresponding complex interplay of collisions and laser light will be investigated in future work.

1. Line assignments

In the following, we outline how we use the knowledge of the spectra to reliably assign individual lines in the recorded fluorescence spectroscopy data.

2. $X(N=0,G=2) \rightarrow A(J'^P=1/2^-)$ spectrum

The spectrum for the transition $X(N=0,G=2) \rightarrow A(J'^P=1/2^-)$ is shown in Fig. 5. This spectrum is relatively simple, with a small number of sublevels. Moreover, the $J'=1/2$ excited states experience no first-order shift from the quadrupole hyperfine interaction, $H_Q^{(\text{Ba})}$. Since the magnetic hyperfine interaction is small compared to the rotational energy splitting, the spectrum can be approximately described using an effective Hamiltonian that operates only on levels with the same value of J'^P. This effective Hamiltonian can be written as

$$H^{\text{eff}}_{J'=1/2} = \left[h^{(\text{Ba})}_{1/2} - d^{(\text{Ba})}\cdot P(-1)^p \cdot \frac{1}{2}(2J+1)\right]\frac{\mathbf{I}^{(\text{Ba})}\cdot\mathbf{J}}{2J(J+1)} + \left[h^{(\text{F})}_{1/2} - d^{(\text{F})}\cdot P(-1)^p \cdot \frac{1}{2}(2J+1)\right]\frac{\mathbf{I}^{(\text{F})}\cdot\mathbf{J}}{2J(J+1)}. \tag{D1}$$

Hence, to first approximation the hyperfine splittings in the $J'^P=1/2^-$ state depend only on the parameters $h^{(\text{Ba})}_{1/2}+d^{(\text{Ba})}$ and $h^{(\text{F})}_{1/2}+d^{(\text{F})}$. Moreover, $h^{(\text{F})}_{1/2}$ and $d^{(\text{F})}$ are known from prior data on ^{138}BaF [46] and give only small ($\lesssim 10\,\text{MHz}$) splittings.

Lines in the high-frequency region ($\approx$350–650 MHz in Fig. 5) clearly originated from the $X(N=0,G=2)$ sublevels. From their relative position and amplitude, the higher-(lower-)frequency cluster of four lines here were assigned to ^{137}BaF (^{135}BaF). The smaller (nearly overlapped) doublet splittings corresponded to expected splittings from the known values of $h^{(\text{F})}_{1/2}$ and $d^{(\text{F})}$ [46], and the average of the larger doublet splittings corresponded to the known ^{19}F hyperfine splittings in the $X^2\Sigma^+$ state. All of these high-frequency lines were assigned to transitions to the maximum value of $F_1'=2$ in the excited state with $J'=1/2$. Next, the largest-amplitude lines in the low-frequency region of this spectrum (the two unresolved doublets near 0 frequency in Fig. 5) were assigned to ^{137}BaF and to transitions to excited states with $F'=1$.

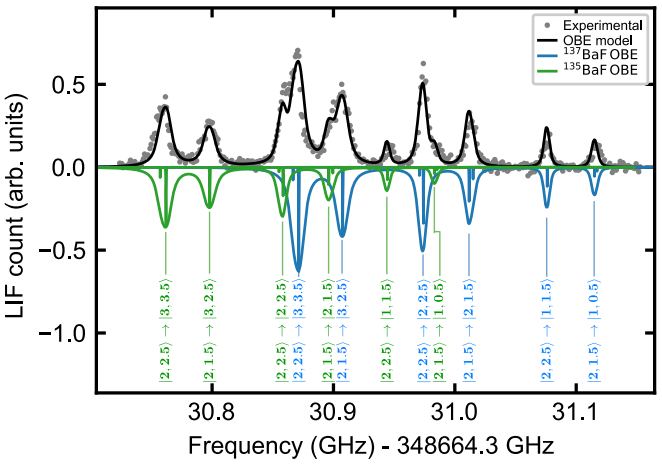

FIG. 7. Spectra for the $X(N=0, G=2) \rightarrow A(J'^{P}=3/2^{-})$ transitions in $^{135/137}$BaF. All notations are as in Fig. 5.

Then peaks were fit to each of the lines assigned to ^{137}BaF to find a preliminary location of the line centers.

Next, pairs of large and relatively isolated lines were identified that originated from a common X state sub-

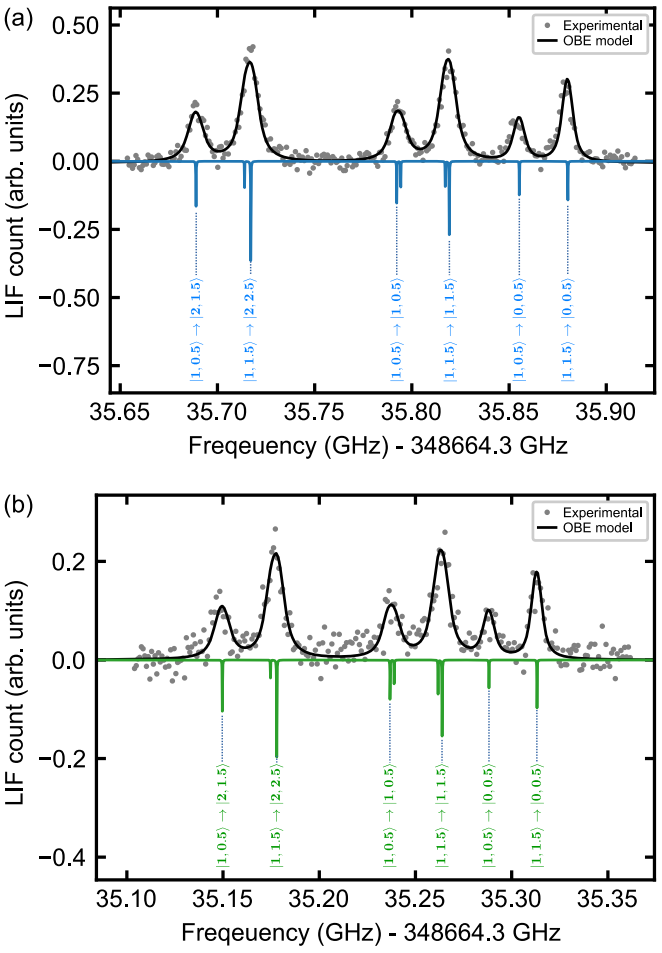

FIG. 8. Spectra for the $X(N=0, G=1) \rightarrow A(J'^{P}=3/2^{-})$ transition. All notations are as in Fig. 5. For this transition, the spectral lines of ^{137}BaF presented in (a) are well separated from the corresponding ^{135}BaF features shown in (b).

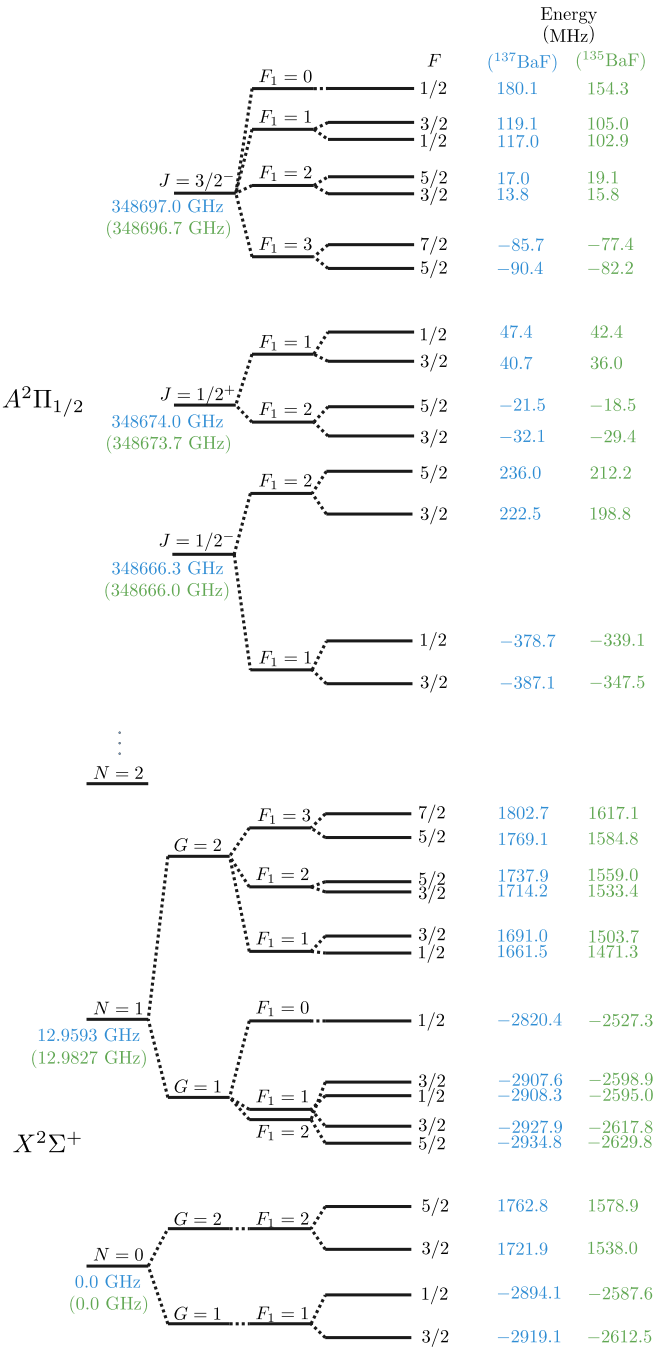

FIG. 9. Energy levels in the lower hyperfine-rotational levels of the $X^2\Sigma^+$ and $A^2\Pi_{1/2}$ states, for the isotopologues ^{137}BaF (blue) ^{135}BaF (green). The hyperfine splittings within the $A^2\Pi_{1/2}$ states are based on the parameters estimated in the current work. The two isotopologues have similar structure of the energy splittings, except for the $|X, N=1, G=1, F_1=1, F=1/2\rangle$ and $|X, N=1, G=1, F_1=2, F=3/2\rangle$ states, where the order of these levels is reversed in the case of ^{135}BaF.

level, but terminated in different excited state sublevels. In Fig. 5 these lines, labeled in bold, corresponded to the transitions $X\,|F_1=2, F=2.5\rangle \rightarrow A\,|F_1=2, F=2.5\rangle$ and $\rightarrow A\,|F_1=1, F=1.5\rangle$; and $X\,|F_1=2, F=1.5\rangle \rightarrow A\,|F_1=2, F=1.5\rangle$ and $\rightarrow A\,|F_1=1, F=0.5\rangle$. By fitting

TABLE IV. List of all transition pairs contributing to extraction of hyperfine Hamiltonian parameters in ^{135}BaF. In all cases, a common initial state connects to two different excited states. Here Δ is splitting between the two excited states; σ_{st} is the purely statistical uncertainty in Δ, after rescaling to account for the global value of χ^2_ν; σ_f is the uncertainty in each line position associated with unresolved overlapping lines and σ_f^Δ is the associated uncertainty in Δ, obtained by adding contributions for each line in quadrature; σ_Z is the uncertainty in each line position associated with Zeeman shifts in the uncalibrated laboratory magnetic field and σ_Z^Δ is the associated uncertainty in Δ, obtained by adding contributions for each line linearly (since they are correlated); σ_{tot} is the total uncertainty in Δ for each transition pair, obtained by adding σ_{st}, σ_Z^Δ, and σ_Z^Δ in quadrature; σ_{tot}^{wt} is the total uncertainty in Δ from a weighted average over all transition pairs that probed the same pair of excited states; and Δ^{wt} is the weighted average value of Δ, used in the final global fit for hyperfine parameters.

Transitions in ^{135}BaF $X\,\lvert N, G, F_1, F\rangle \rightarrow A\,\lvert J'^P, F_1', F'\rangle$	Δ (MHz)	σ_{st} (MHz)	σ_f (MHz)	σ_f^Δ (MHz)	σ_Z (MHz)	σ_Z^Δ (MHz)	σ_{tot} (MHz)	σ_{tot}^{wt} (MHz)	Δ^{wt} (MHz)
$\lvert 0,2,2,2.5\rangle \rightarrow \lvert 3/2^-,3,3.5\rangle$	98.62	1.55	0.42	0.47	0.76	1.48	2.19	2.19	98.62
$\lvert 0,2,2,2.5\rangle \rightarrow \lvert 3/2^-,2,2.5\rangle$			0.22		0.72				
$\lvert 0,2,2,1.5\rangle \rightarrow \lvert 3/2^-,3,2.5\rangle$	97.13	1.42	–	0.74	0.70	1.34	2.09	2.09	97.13
$\lvert 0,2,2,1.5\rangle \rightarrow \lvert 3/2^-,2,1.5\rangle$			0.74		0.65				
$\lvert 0,2,2,2.5\rangle \rightarrow \lvert 3/2^-,2,2.5\rangle$	83.61	1.54	0.22	0.22	0.72	1.39	2.08	1.50	84.89
$\lvert 0,2,2,2.5\rangle \rightarrow \lvert 3/2^-,1,1.5\rangle$			–		0.67				
$\lvert 0,1,1,1.5\rangle \rightarrow \lvert 3/2^-,2,2.5\rangle$	86.30	1.90	0.52	0.71	0.41	0.78	2.17		
$\lvert 0,1,1,1.5\rangle \rightarrow \lvert 3/2^-,1,1.5\rangle$			0.48		0.37				
$\lvert 0,2,2,1.5\rangle \rightarrow \lvert 3/2^-,2,1.5\rangle$	88.12	1.51	0.74	0.96	0.65	1.24	2.17	1.57	88.29
$\lvert 0,2,2,1.5\rangle \rightarrow \lvert 3/2^-,1,0.5\rangle$			0.61		0.59				
$\lvert 0,1,1,0.5\rangle \rightarrow \lvert 3/2^-,2,1.5\rangle$	88.49	2.11	–	0.7	0.29	0.53	2.29		
$\lvert 0,1,1,0.5\rangle \rightarrow \lvert 3/2^-,1,0.5\rangle$			0.70		0.24				
$\lvert 0,1,1,0.5\rangle \rightarrow \lvert 3/2^-,1,0.5\rangle$	50.25	0.84	0.7	0.7	0.24	0.46	1.18	1.18	50.25
$\lvert 0,1,1,0.5\rangle \rightarrow \lvert 3/2^-,0,0.5\rangle$			–		0.22				
$\lvert 0,1,1,1.5\rangle \rightarrow \lvert 3/2^-,1,1.5\rangle$	49.48	1.41	0.48	0.48	0.37	0.69	1.64	1.64	49.48
$\lvert 0,1,1,1.5\rangle \rightarrow \lvert 3/2^-,0,0.5\rangle$			–		0.33				
$\lvert 0,2,2,2.5\rangle \rightarrow \lvert 1/2^-,2,2.5\rangle$	560.22	5.01	–	–	1.33	2.6	5.64	5.64	560.22
$\lvert 0,2,2,2.5\rangle \rightarrow \lvert 1/2^-,1,1.5\rangle$			–		1.28				
$\lvert 0,2,2,1.5\rangle \rightarrow \lvert 1/2^-,2,1.5\rangle$	537.94	3.82	–	–	1.27	2.47	4.55	4.55	537.94
$\lvert 0,2,2,1.5\rangle \rightarrow \lvert 1/2^-,1,0.5\rangle$			–		1.20				

to $H^{\text{eff}}_{J'=1/2}$, these splittings yielded a preliminary value of $h^{(\text{Ba})}_{1/2} + d^{(\text{Ba})}$ for ^{137}BaF, accurate to a few MHz.

From the expected scaling of $h^{(\text{Ba})}_{1/2} + d^{(\text{Ba})}$ with the nuclear magnetic moment $\mu^{(\text{Ba})}$, we could then estimate the splittings of the ^{135}BaF lines for transitions to excited states with $F' = 1$. In the spectrum of Fig. 5 these clearly overlapped with another set of lines, which were later assigned to transitions $X(N=1, G=1) \rightarrow A(J'^P = 1/2^+)$. However, two pairs of sufficiently large and isolated lines were identified to enable preliminary estimates of $h^{(\text{Ba})}_{1/2} + d^{(\text{Ba})}$ for ^{135}BaF (independent of the values from ^{137}BaF) from this spectrum as well.

3. $X(N = 1, G = 2) \rightarrow A(J'^P = 1/2^+)$ spectrum

The $X(N=1, G=2) \rightarrow A(J'^P = 1/2^+)$ transitions with lines identified by their quantum numbers are shown in Fig. 6. The largest lines on the high-frequency side of the spectrum were tentatively assigned to transitions in ^{137}BaF with the strongest transition dipole matrix elements. Line positions and further line assignments for both isotopologues then proceeded as described above. This analysis was used to determine a preliminary value of $h^{(\text{Ba})}_{1/2} - d^{(\text{Ba})}$ for ^{137}BaF. (Lines in this spectrum were only used for estimation of hyperfine parameters in ^{137}BaF, not in ^{135}BaF.) With the preliminary value of $h^{(\text{Ba})}_{1/2} - d^{(\text{Ba})}$, it was possible to estimate the positions of the $X(N=1, G=1) \rightarrow A(J'^P = 1/2^+)$ transitions for ^{137}BaF and assign the "extra" lines in Fig. 5 to them.

4. $X(N = 0, G = 2, 1) \rightarrow A(J'^P = 3/2^-)$ spectra

The spectrum of $X(N=0, G=2) \rightarrow A(J'^P = 3/2^-)$ transitions is shown in Fig. 7 for both isotopologues. The $X(N=0, G=1) \rightarrow A(J'^P = 3/2^-)$ spectra for ^{137}BaF and ^{135}BaF are shown in Figs. 8(a) and 8(b), respectively. These measurements, together with the preliminary evaluations of $h^{(\text{Ba})}_{1/2}$ and $d^{(\text{Ba})}$, made it possible to determine the values of $eq_0Q^{(\text{Ba})}$ for the two isotopologues.

5. Global analysis of the hyperfine structure and uncertainty budget

After all lines were assigned and preliminary fits performed to find values of hyperfine Hamiltonian parameters, a final global fit to all line pairs used in the preliminary analysis of each spectrum scan was performed, including the effect of Hamiltonian matrix elements off-diagonal in J'.

For each fitted level splitting, a statistical uncertainty (typically 1–4 MHz) was assigned from the standard error in the mean between nominally identical spectrum scans. The reduced chi-squared value of this global fit was $\chi^2_\nu = 1.7\ (2.1)$ for ^{137}BaF (^{135}BaF). The final statistical uncertainties for each splitting were assigned by multiplying the raw uncertainty by the corresponding value of $\sqrt{\chi^2_\nu}$ for each isotopologue. An systematic uncertainty of up to 0.7 MHz was added to some lines to account for the effect of unresolved overlaps with smaller nearby lines. An additional systematic uncertainty,

TABLE V. List of all transition pairs contributing to extraction of hyperfine Hamiltonian parameters in ^{137}BaF. All notations are the same as in Table IV.

Transition in ^{137}BaF $X\,\lvert N, G, F_1, F\rangle \rightarrow A\,\lvert J'^P, F_1', F'\rangle$	Δ (MHz)	σ_{st} (MHz)	σ_f (MHz)	σ_f^{Δ} (MHz)	σ_Z (MHz)	σ_Z^{Δ} (MHz)	σ_{tot} (MHz)	σ_{tot}^{wt} (MHz)	Δ^{wt} (MHz)
$\lvert 0,2,2,2.5\rangle \rightarrow \lvert 3/2^-,3,3.5\rangle$	101.59	1.11	0.44	0.51	0.76	1.48	1.92	1.92	101.59
$\lvert 0,2,2,2.5\rangle \rightarrow \lvert 3/2^-,2,2.5\rangle$			0.25		0.72				
$\lvert 0,2,2,1.5\rangle \rightarrow \lvert 3/2^-,3,2.5\rangle$	104.67	1.07	–	0.5	0.70	1.34	1.78	1.78	104.67
$\lvert 0,2,2,1.5\rangle \rightarrow \lvert 3/2^-,2,1.5\rangle$			0.5		0.65				
$\lvert 0,2,2,2.5\rangle \rightarrow \lvert 3/2^-,2,2.5\rangle$	102.17	0.93	0.25	0.25	0.72	1.39	1.69	1.14	101.60
$\lvert 0,2,2,2.5\rangle \rightarrow \lvert 3/2^-,1,1.5\rangle$			–		0.67				
$\lvert 0,1,1,1.5\rangle \rightarrow \lvert 3/2^-,2,2.5\rangle$	101.13	1.15	0.48	0.66	0.41	0.78	1.54		
$\lvert 0,1,1,1.5\rangle \rightarrow \lvert 3/2^-,1,1.5\rangle$			0.45		0.37				
$\lvert 0,2,2,1.5\rangle \rightarrow \lvert 3/2^-,2,1.5\rangle$	103.34	0.88	0.5	0.66	0.65	1.24	1.66	1.02	103.68
$\lvert 0,2,2,1.5\rangle \rightarrow \lvert 3/2^-,1,0.5\rangle$			0.43		0.59				
$\lvert 0,1,1,0.5\rangle \rightarrow \lvert 3/2^-,2,1.5\rangle$	103.89	0.97	–	0.67	0.29	0.52	1.29		
$\lvert 0,1,1,0.5\rangle \rightarrow \lvert 3/2^-,1,0.5\rangle$			0.67		0.23				
$\lvert 0,1,1,0.5\rangle \rightarrow \lvert 3/2^-,1,0.5\rangle$	61.57	0.66	0.67	0.67	0.23	0.44	1.04	1.04	61.57
$\lvert 0,1,1,0.5\rangle \rightarrow \lvert 3/2^-,0,0.5\rangle$			–		0.21				
$\lvert 0,1,1,1.5\rangle \rightarrow \lvert 3/2^-,1,1.5\rangle$	60.97	0.41	0.45	0.45	0.37	0.69	0.91	0.91	60.97
$\lvert 0,1,1,1.5\rangle \rightarrow \lvert 3/2^-,0,0.5\rangle$			–		0.32				
$\lvert 0,2,2,2.5\rangle \rightarrow \lvert 1/2^-,2,2.5\rangle$	625.38	4.76	–	–	1.46	2.86	5.55	5.55	625.38
$\lvert 0,2,2,2.5\rangle \rightarrow \lvert 1/2^-,1,1.5\rangle$			–		1.41				
$\lvert 0,2,2,1.5\rangle \rightarrow \lvert 1/2^-,2,1.5\rangle$	602.78	4.19	–	–	1.39	2.72	4.99	4.99	602.78
$\lvert 0,2,2,1.5\rangle \rightarrow \lvert 1/2^-,1,0.5\rangle$			–		1.33				
$\lvert 1,2,3,2.5\rangle \rightarrow \lvert 1/2^+,2,1.5\rangle$	74.41	2.24	–	–	0.72	1.38	2.63	1.50	74.25
$\lvert 1,2,3,2.5\rangle \rightarrow \lvert 1/2^+,1,1.5\rangle$			–		0.66				
$\lvert 1,1,2,1.5\rangle \rightarrow \lvert 1/2^+,2,1.5\rangle$	74.18	1.16	0.45	1.32	0.28	0.51	1.83		
$\lvert 1,1,2,1.5\rangle \rightarrow \lvert 1/2^+,1,1.5\rangle$			1.24		0.23				
$\lvert 1,2,2,2.5\rangle \rightarrow \lvert 1/2^+,2,2.5\rangle$	61.8	1.40	–	–	0.62	1.16	1.82	1.24	62.35
$\lvert 1,2,2,2.5\rangle \rightarrow \lvert 1/2^+,1,1.5\rangle$			–		0.54				
$\lvert 1,1,2,2.5\rangle \rightarrow \lvert 1/2^+,2,2.5\rangle$	62.83	1.47	–	0.25	0.44	0.80	1.69		
$\lvert 1,1,2,2.5\rangle \rightarrow \lvert 1/2^+,1,1.5\rangle$			0.25		0.36				
$\lvert 1,2,1,1.5\rangle \rightarrow \lvert 1/2^+,2,2.5\rangle$	68.48	1.32	–	–	0.52	0.95	1.63	1.63	68.48
$\lvert 1,2,1,1.5\rangle \rightarrow \lvert 1/2^+,1,0.5\rangle$			–		0.43				

in the range 0.4–2.8 MHz, was assigned to each line due to possible Zeeman shifts from the laboratory magnetic field (roughly earth's field).

Figure 9 shows the final assigned energies of all states used in the analysis of hyperfine splittings, complementing Fig. 1.

All transition pairs used to determine the parameters of the hyperfine Hamiltonian are shown in Tables IV and V, for ^{135}BaF and ^{137}BaF, respectively. These tables show the quantum numbers for each line, the value of the splitting between excited states in the transition pair, and the statistical uncertainty (after correction for $\chi_\nu^2 > 1$) of each splitting.

We also account for two sources of systematic errors. The first arises from apparent line shifts due to unresolved overlapping spectral lines. To account for this, we fit the OBE-modeled spectra using the same procedure as for the real data, then calculate the difference between the fitted level splitting and the splitting known directly from the Hamiltonian eigenvalues. Note that some lines are sufficiently isolated so that this results in no error. For lines with substantial overlap, the resulting errors are in the range 0.2–0.7 MHz.

The second source of possible systematic error arises from Zeeman shifts due to the nonzero magnetic field in the laboratory used for the fluorescence measurements, which was measured to be about 0.45 G (0.17 G) perpendicular (parallel) to the linear polarization of the laser beam. Using known magnetic g factors of the $X^2\Sigma$ [18] and $A^2\Pi_{1/2}$ [42] states and the diagonalized hyperfine/rotation Hamiltonian, we calculated Zeeman shifts in the energy of each state used in the analysis. We conservatively assume that the error in the observed state energy could be as large as half the maximum splitting between m_F sublevels in the state. The total systematic error in the measurement of the position of each of the transitions is assigned by linearly adding errors from Zeeman shifts in the ground and excited states.

APPENDIX E: ANALYSIS OF THE ABSORPTION SPECTROSCOPY DATA

The analysis of absorption spectroscopy data has been discussed in detail in previous work [26,27]. Here we follow the same procedures, with adaptations as needed for the detection of low-abundance isotopologues.

1. Data acquisition

As molecular formation is based on a pulsed ablation process, a continuous scan of the probe laser—as common in room-temperature vapor cell experiments—is not possible,

and thus an incremental frequency scan is used. For each frequency step, a time-resolved absorption trace is recorded, the signal is integrated over specific time intervals, and averaged over typically four repetitions to reduce signal fluctuations [27]. By combining these data and applying a moving average filter for smoothing, we obtain distinct spectra across multiple time intervals, with later times corresponding to well-thermalized molecules. We then choose the latest time interval for which the signal-to-noise ratio of the decaying absorption signal still allows for detecting all smaller pronounced peaks, which are later associated with lower-abundance isotopologues.

For frequency ranges that span more than a few GHz, a single scan is not feasible due to the limited time window during which the dewar-style cryostat employed for the absorption spectroscopy measurements can maintain cold temperatures, the restricted mode-hop-free tuning range of the laser, and signal degradation caused by prolonged ablation at a fixed target position. To overcome these limitations, successive scans were performed over smaller, slightly overlapping frequency ranges. These segments are later stitched together, accounting for variations in the molecular signal arising from target degradation.

The laser frequency is recorded using a wavemeter whose frequency is regularly validated against cesium and rubidium vapor lines, the BaF cooling transition [29], and a frequency-stabilized HeNe laser [26], achieving an absolute accuracy of better than 50 MHz, smaller than the uncertainty arising from the inherent molecular dynamics in the buffer gas cell.

2. Fitting molecular constants

The determination of the rovibrational constants begins with fixing the well-established constants of the bosonic isotopologues ^{138}BaF and ^{136}BaF with a simple structure and clearly pronounced transition lines [26]. In the next step, these constants are scaled for the less abundant isotopologues (^{137}BaF, ^{135}BaF, and ^{134}BaF) and combined with the hyperfine constants of the excited state $A^2\Pi_{1/2}$ extracted from fluorescence spectroscopy.

Typically, 10 to 20 prominent peaks in the measured spectra can be unambiguously matched to those from the theoretical model. For each isotopologue and each vibrational transition $X^2\Sigma^+(\nu) \rightarrow A^2\Pi_{1/2}(\nu')$, we then determine an individual energy offset $T_{\nu',\nu} = T'_\nu - T_\nu$ by minimizing the least-squared error between the peak positions between these experimental and theoretical transitions. Finally, applying these offsets in the relation $T_\nu = T_e + \omega_e(\nu + 1/2) - \omega_e\chi_e(\nu + 1/2)^2 + \omega_e y_e(\nu + 1/2)^3$, the vibrational constants ω_e, ω'_e and T'_e are extracted using least-square fits, while the remaining constants are fixed from isotope scalings, as summarized in Table III.

[1] M. S. Safronova, D. Budker, D. DeMille, D. F. J. Kimball, A. Derevianko, and C. W. Clark, Search for new physics with atoms and molecules, Rev. Mod. Phys. **90**, 025008 (2018).

[2] D. DeMille, N. R. Hutzler, A. M. Rey, and T. Zelevinsky, Quantum sensing and metrology for fundamental physics with molecules, Nat. Phys. **20**, 741 (2024).

[3] J. J. Hudson, B. E. Sauer, M. R. Tarbutt, and E. A. Hinds, Measurement of the electron electric dipole moment using YbF molecules, Phys. Rev. Lett. **89**, 023003 (2002).

[4] V. Andreev, D. G. Ang, D. DeMille, J. M. Doyle, G. Gabrielse, J. Haefner, N. R. Hutzler, Z. Lasner, C. Meisenhelder, B. R. O'Leary *et al.* (ACME Collaboration), Improved limit on the electric dipole moment of the electron, Nature (London) **562**, 355 (2018).

[5] T. S. Roussy, L. Caldwell, T. Wright, W. B. Cairncross, Y. Shagam, K. B. Ng, N. Schlossberger, S. Y. Park, A. Wang, J. Ye, and E. A. Cornell, An improved bound on the electron's electric dipole moment, Science **381**, 46 (2023).

[6] O. Grasdijk, O. Timgren, J. Kastelic, T. Wright, S. Lamoreaux, D. DeMille, K. Wenz, M. Aitken, T. Zelevinsky, T. Winick, and D. Kawall, Centrex: A new search for time-reversal symmetry violation in the ^{205}Tl nucleus, Quantum Sci. Technol. **6**, 044007 (2021).

[7] V. V. Flambaum, D. DeMille, and M. G. Kozlov, Time-reversal symmetry violation in molecules induced by nuclear magnetic quadrupole moments, Phys. Rev. Lett. **113**, 103003 (2014).

[8] A. Shelkovnikov, R. J. Butcher, C. Chardonnet, and A. Amy-Klein, Stability of the proton-to-electron mass ratio, Phys. Rev. Lett. **100**, 150801 (2008).

[9] H. L. Bethlem and W. Ubachs, Testing the time-invariance of fundamental constants using microwave spectroscopy on cold diatomic radicals, Faraday Discuss. **142**, 25 (2009).

[10] S. Truppe, R. J. Hendricks, S. K. Tokunaga, H. J. Lewandowski, M. G. Kozlov, C. Henkel, E. A. Hinds, and M. R. Tarbutt, A search for varying fundamental constants using Hertz-level frequency measurements of cold ch molecules, Nat. Commun. **4**, 2600 (2013).

[11] S. Schiller, D. Bakalov, and V. I. Korobov, Simplest molecules as candidates for precise optical clocks, Phys. Rev. Lett. **113**, 023004 (2014).

[12] J. Kobayashi, A. Ogino, and S. Inouye, Measurement of the variation of electron-to-proton mass ratio using ultracold molecules produced from laser-cooled atoms, Nat. Commun. **10**, 3771 (2019).

[13] K. H. Leung, B. Iritani, E. Tiberi, I. Majewska, M. Borkowski, R. Moszynski, and T. Zelevinsky, Terahertz vibrational molecular clock with systematic uncertainty at the 10^{-14} level, Phys. Rev. X **13**, 011047 (2023).

[14] M. Athanasakis-Kaklamanakis, S. G. Wilkins, A. A. Breier, and G. Neyens, King-plot analysis of isotope shifts in simple diatomic molecules, Phys. Rev. X **13**, 011015 (2023).

[15] S. G. Wilkins, S. M. Udrescu, M. Athanasakis-Kaklamanakis, R. F. G. Ruiz, M. Au, I. Belosevic, R. Berger, M. L. Bissell, A. A. Breier, A. J. Brinson, *et al.*, Observation of the distribution of nuclear magnetization in a molecule, arXiv:2311.04121.

[16] S. M. Udrescu, S. G. Wilkins, A. A. Breier, M. Athanasakis-Kaklamanakis, R. F. Garcia Ruiz, M. Au, I. Belošević, R. Berger, M. L. Bissell, C. L. Binnersley

et al., Precision spectroscopy and laser-cooling scheme of a radium-containing molecule, Nat. Phys. **20**, 202 (2024).

[17] D. DeMille, S. B. Cahn, D. Murphree, D. A. Rahmlow, and M. G. Kozlov, Using molecules to measure nuclear spin-dependent parity violation, Phys. Rev. Lett. **100**, 023003 (2008).

[18] S. B. Cahn, J. Ammon, E. Kirilov, Y. V. Gurevich, D. Murphree, R. Paolino, D. A. Rahmlow, M. G. Kozlov, and D. DeMille, Zeeman-tuned rotational level-crossing spectroscopy in a diatomic free radical, Phys. Rev. Lett. **112**, 163002 (2014).

[19] E. B. Norrgard, D. S. Barker, S. Eckel, J. A. Fedchak, N. N. Klimov, and J. Scherschligt, Nuclear-spin dependent parity violation in optically trapped polyatomic molecules, Commun. Phys. **2**, 77 (2019).

[20] J. Lim, J. R. Almond, M. A. Trigatzis, J. A. Devlin, N. J. Fitch, B. E. Sauer, M. R. Tarbutt, and E. A. Hinds, Laser cooled YbF molecules for measuring the electron's electric dipole moment, Phys. Rev. Lett. **120**, 123201 (2018).

[21] N. J. Fitch, J. Lim, E. A. Hinds, B. E. Sauer, and M. R. Tarbutt, Methods for measuring the electron's electric dipole moment using ultracold YbF molecules, Quantum Sci. Technol. **6**, 014006 (2021).

[22] I. Kozyryev and N. R. Hutzler, Precision measurement of time-reversal symmetry violation with laser-cooled polyatomic molecules, Phys. Rev. Lett. **119**, 133002 (2017).

[23] P. Aggarwal, H. L. Bethlem, A. Borschevsky, M. Denis, K. Esajas, P. A. B. Haase, Y. Hao, S. Hoekstra, K. Jungmann, T. B. Meijknecht *et al.*, Measuring the electric dipole moment of the electron in BaF, Eur. Phys. J. D **72**, 197 (2018).

[24] N. Fitch and M. R. Tarbutt, Laser-cooled molecules, Adv. At. Mol. Opt. **70**, 157 (2021).

[25] T. Langen, G. Valtolina, D. Wang, and J. Ye, Quantum state manipulation and cooling of ultracold molecules, Nat. Phys. **20**, 702 (2024).

[26] M. Rockenhäuser, F. Kogel, E. Pultinevicius, and T. Langen, Absorption spectroscopy for laser cooling and high-fidelity detection of barium monofluoride molecules, Phys. Rev. A **108**, 062812 (2023).

[27] R. Albrecht, M. Scharwaechter, T. Sixt, L. Hofer, and T. Langen, Buffer-gas cooling, high-resolution spectroscopy, and optical cycling of barium monofluoride molecules, Phys. Rev. A **101**, 013413 (2020).

[28] T. Chen, W. Bu, and B. Yan, Radiative deflection of a BaF molecular beam via optical cycling, Phys. Rev. A **96**, 053401 (2017).

[29] M. Rockenhäuser, F. Kogel, T. Garg, S. A. Morales-Ramírez, and T. Langen, Laser cooling of barium monofluoride molecules using synthesized optical spectra, Phys. Rev. Res. **6**, 043161 (2024).

[30] F. Kogel, T. Garg, M. Rockenhäuser, S. A. Morales-Ramírez, and T. Langen, Molecular laser cooling using serrodynes: Implementation, characterization and prospects, New J. Phys. **27**, 055001 (2025).

[31] Z. Zeng, S. Deng, S. Yang, and B. Yan, Three-dimensional magneto-optical trapping of barium monofluoride, Phys. Rev. Lett. **133**, 143404 (2024).

[32] F. Kogel, T. Garg, M. Rockenhäuser, S. A. Morales-Ramírez, and T. Langen, Isotopologue-selective laser cooling of molecules, New J. Phys. **27**, 013001 (2025).

[33] F. Kogel, T. Garg, M. Rockenhäuser, and T. Langen, Laser-cooled ^{137}BaF molecules for measuring nuclear-spin-dependent parity violation, Phys. Rev. Res. **7**, L022041 (2025).

[34] A. Boeschoten, V. R. Marshall, T. B. Meijknecht, A. Touwen, H. L. Bethlem, A. Borschevsky, S. Hoekstra, J. W. F. van Hofslot, K. Jungmann, M. C. Mooij *et al.* (NL-*e*EDM Collaboration), Spin-precession method for sensitive electric dipole moment searches, Phys. Rev. A **110**, L010801 (2024).

[35] E. Altuntaş, J. Ammon, S. B. Cahn, and D. DeMille, Demonstration of a sensitive method to measure nuclear-spin-dependent parity violation, Phys. Rev. Lett. **120**, 142501 (2018).

[36] W. R. Phillips, I. Ahmad, H. Emling, R. Holzmann, R. V. F. Janssens, T. L. Khoo, and M. W. Drigert, Octupole deformation in neutron-rich barium isotopes, Phys. Rev. Lett. **57**, 3257 (1986).

[37] G. Arrowsmith-Kron, M. Athanasakis-Kaklamanakis, M. Au, J. Ballof, R. Berger, A. Borschevsky, A. A. Breier, F. Buchinger, D. Budker, L. Caldwell *et al.*, Opportunities for fundamental physics research with radioactive molecules, Rep. Prog. Phys. **87**, 084301 (2024).

[38] W. Bu, Y. Zhang, Q. Liang, T. Chen, and B. Yan, Saturated absorption spectroscopy of buffer-gas-cooled barium monofluoride molecules, Front. Phys. **17**, 62502 (2022).

[39] C. Ryzlewicz and T. Törring, Formation and microwave spectrum of the $^2\Sigma$ radical barium monofluoride, Chem. Phys. **51**, 329 (1980).

[40] C. Effantin, A. Bernard, J. d'Incan, G. Wannous, J. Vergès, and R. Barrow, Studies of the electronic states of the BaF molecule, Mol. Phys. **70**, 735 (1990).

[41] W. E. Ernst, J. Kändler, and T. Törring, Hyperfine structure and electric dipole moment of BaF $X\ ^2\Sigma^+$, J. Chem. Phys. **84**, 4769 (1986).

[42] T. C. Steimle, S. Frey, A. Le, D. DeMille, D. A. Rahmlow, and C. Linton, Molecular-beam optical Stark and Zeeman study of the $A^2\Pi$–$X^2\Sigma^+$ (0,0) band system of BaF, Phys. Rev. A **84**, 012508 (2011).

[43] A. Preston, G. Aufderheide, W. Ballard, R. Mawhorter, and J.-U. Grabow, Global isotopic analysis of rotational spectroscopic data for barium monofluoride, BaF, arXiv:2503.21688.

[44] F. Kogel, M. Rockenhäuser, R. Albrecht, and T. Langen, A laser cooling scheme for precision measurements using fermionic barium monofluoride (^{137}Ba^{19}F) molecules, New J. Phys. **23**, 095003 (2021).

[45] E. Altuntaş, J. Ammon, S. B. Cahn, and D. DeMille, Measuring nuclear-spin-dependent parity violation with molecules: Experimental methods and analysis of systematic errors, Phys. Rev. A **97**, 042101 (2018).

[46] M. Denis, P. A. Haase, M. C. Mooij, Y. Chamorro, P. Aggarwal, H. L. Bethlem, A. Boeschoten, A. Borschevsky, K. Esajas, Y. Hao *et al.*, Benchmarking of the Fock-space coupled-cluster method and uncertainty estimation: Magnetic hyperfine interaction in the excited state of BaF, Phys. Rev. A **105**, 052811 (2022).

[47] N. R. Hutzler, M. F. Parsons, Y. V. Gurevich, P. W. Hess, E. Petrik, B. Spaun, A. C. Vutha, D. DeMille, G. Gabrielse, and J. M. Doyle, A cryogenic beam of refractory, chemically reactive molecules with expansion cooling, Phys. Chem. Chem. Phys. **13**, 18976 (2011).

[48] N. R. Hutzler, H.-I. Lu, and J. M. Doyle, The buffer gas beam: An intense, cold, and slow source for atoms and molecules, Chem. Rev. **112**, 4803 (2012).

[49] W. Bu, T. Chen, G. Lv, and B. Yan, Cold collision and high-resolution spectroscopy of buffer-gas-cooled BaF molecules, Phys. Rev. A **95**, 032701 (2017).

[50] W. Z. Zhao, J. E. Simsarian, L. A. Orozco, and G. D. Sprouse, A computer-based digital feedback control of frequency drift of multiple lasers, Rev. Sci. Instrum. **69**, 3737 (1998).

[51] E. Gomez, S. Aubin, L. A. Orozco, and G. D. Sprouse, Lifetime and hyperfine splitting measurements on the 7*s* and 6*p* levels in rubidium, J. Opt. Soc. Am. B **21**, 2058 (2004).

[52] D. Rahmlow, Towards a measurement of parity nonconservation in diatomic molecules, Ph.D. thesis, Yale University, 2010.

[53] K. Shimizu and F. Shimizu, Laser induced fluorescence spectra of the a $^3\Pi_u$-$X\,^1\Sigma^+{}_g$ band of Na_2 by molecular beam, J. Chem. Phys. **78**, 1126 (1983).

[54] C. Ryzlewicz, H.-U. Schütze-Pahlmann, J. Hoeft, and T. Törring, Rotational spectrum and hyperfine structure of the $^2\Sigma$ radicals BaF and BaCl, Chem. Phys. **71**, 389 (1982).

[55] R. H. Hay, The nuclear magnetic moments of C^{13}, Ba^{135} and Ba^{137}, Phys. Rev. **60**, 75 (1941).

[56] P. Pyykkö, Year-2008 nuclear quadrupole moments, Mol. Phys. **106**, 1965 (2008).

[57] Y. Hao, M. Ilias, E. Eliav, P. Schwerdtfeger, V. V. Flambaum, and A. Borschevsky, Nuclear anapole moment interaction in BaF from relativistic coupled-cluster theory, Phys. Rev. A **98**, 032510 (2018).

[58] M. Denis, P. A. B. Haase, R. G. E. Timmermans, E. Eliav, N. R. Hutzler, and A. Borschevsky, Enhancement factor for the electric dipole moment of the electron in the BaOH and YbOH molecules, Phys. Rev. A **99**, 042512 (2019).

[59] M. Denis, Y. Hao, E. Eliav, N. R. Hutzler, M. K. Nayak, R. G. E. Timmermans, and A. Borschesvky, Enhanced $\mathcal{P}$, $\mathcal{T}$-violating nuclear magnetic quadrupole moment effects in laser-coolable molecules, J. Chem. Phys. **152**, 084303 (2020).

[60] P. A. B. Haase, D. J. Doeglas, A. Boeschoten, E. Eliav, M. Ilias, P. Aggarwal, H. L. Bethlem, A. Borschevsky, K. Esajas, Y. Hao, S. Hoekstra, V. R. Marshall, T. B. Meijknecht, M. C. Mooij, K. Steinebach, R. G. E. Timmermans, A. P. Touwen, W. Ubachs, L. Willmann, Y. Yin *et al.*, Systematic study and uncertainty evaluation of $\mathcal{P}$, $\mathcal{T}$-odd molecular enhancement factors in baf, J. Chem. Phys. **155**, 034309 (2021).

[61] DIRAC, a relativistic *ab initio* electronic structure program, Release DIRAC19 (2019), written by A. S. P. Gomes, T. Saue, L. Visscher, H. J. Aa. Jensen, and R. Bast, with contributions from I. A. Aucar, V. Bakken, K. G. Dyall, S. Dubillard, U. Ekström, E. Eliav, T. Enevoldsen, E. Faßhauer, T. Fleig, O. Fossgaard, L. Halbert, E. D. Hedegård, B. Heimlich-Paris, T. Helgaker, J. Henriksson, M. Ilias, R. Ch. Jacob, S. Knecht, S. Komorovský, O. Kullie *et al.* http://dx.doi.org/10.5281/zenodo.3572669; see also http://www.diracprogram.org.

[62] T. Saue, R. Bast, A. S. P. Gomes, H. J. A. Jensen, L. Visscher, I. A. Aucar, R. Di Remigio, K. G. Dyall, E. Eliav, E. Fasshauer *et al.*, The Dirac code for relativistic molecular calculations, J. Chem. Phys. **152**, 204104 (2020).

[63] K. G. Dyall, Relativistic double-zeta, triple-zeta, and quadruple-zeta basis sets for the 4*s*, 5*s*, 6*s*, and 7*s* elements, J. Phys. Chem. A **113**, 12638 (2009).

[64] K. G. Dyall, Core correlating basis functions for elements 31–118, Theor. Chem. Acc. **131**, 1217 (2012).

[65] K. G. Dyall, Relativistic double-zeta, triple-zeta, and quadruple-zeta basis sets for the light elements H–Ar, Theor. Chem. Acc. **135**, 128 (2016).

[66] Y. Chamorro, F. Kogel, T. Langen, and A. Borschevsky, following paper, Magnetic hyperfine structure constants of ^{137}BaF in the $^2\Pi_{1/2}$ and $^2\Pi_{3/2}$ excited states, Phys. Rev. A **112**, 042808 (2025).

[67] D. Leimbach, J. Karls, Y. Guo, R. Ahmed, J. Ballof, L. Bengtsson, F. Boix Pamies, A. Borschevsky, K. Chrysalidis, E. Eliav *et al.*, The electron affinity of astatine, Nat. Commun. **11**, 3824 (2020).

[68] P. A. Haase, E. Eliav, M. Ilias, and A. Borschevsky, Hyperfine structure constants on the relativistic coupled cluster level with associated uncertainties, J. Phys. Chem. A **124**, 3157 (2020).

[69] A. Hiramoto, M. Baba, K. Enomoto, K. Iwakuni, S. Kuma, Y. Takahashi, R. Tobaru, and Y. Miyamoto, Measurement of doppler effects in a cryogenic buffer-gas cell, Phys. Rev. A **107**, 043114 (2023).

[70] G. Fricke and K. Heilig, *Nuclear Charge Radii 56-Ba Barium: Datasheet from Landolt-Börnstein - Group I Elementary Particles, Nuclei and Atoms, Vol. 20: "Nuclear Charge Radii" in Springer Materials* (Springer-Verlag, Berlin, Heidelberg, 2004).

[71] W. H. King, *Isotope Shifts in Atomic Spectra* (Springer Science & Business Media, New York, 2013).

[72] F. Gebert, Y. Wan, F. Wolf, C. N. Angstmann, J. C. Berengut, and P. O. Schmidt, Precision isotope shift measurements in calcium ions using quantum logic detection schemes, Phys. Rev. Lett. **115**, 053003 (2015).

[73] K. Ono, Y. Saito, T. Ishiyama, T. Higomoto, T. Takano, Y. Takasu, Y. Yamamoto, M. Tanaka, and Y. Takahashi, Observation of nonlinearity of generalized King plot in the search for new boson, Phys. Rev. X **12**, 021033 (2022).

[74] J. Hur, D. P. L. Aude Craik, I. Counts, E. Knyazev, L. Caldwell, C. Leung, S. Pandey, J. C. Berengut, A. Geddes, W. Nazarewicz *et al.*, Evidence of two-source King plot nonlinearity in spectroscopic search for new boson, Phys. Rev. Lett. **128**, 163201 (2022).

[75] L. R. Hunter, S. E. Maxwell, K. A. Ulmer, N. D. Charney, S. K. Peck, D. Krause, Jr., S. Ter-Avetisyan, and D. DeMille, Detailed spectroscopy of the $a(1)[^3\Sigma^+]$ state of PbO, Phys. Rev. A **65**, 030501(R) (2002).

[76] J. C. Harms, L. C. O'Brien, and J. J. O'Brien, Mass-independent dunham analysis of the known electronic states of platinum sulfide, PtS, and analysis of the electronic field-shift effect, J. Chem. Phys. **151**, 094303 (2019).

[77] S. M. Udrescu, A. J. Brinson, R. F. G. Ruiz, K. Gaul, R. Berger, J. Billowes, C. L. Binnersley, M. L. Bissell, A. A. Breier, K. Chrysalidis *et al.*, Isotope shifts of radium monofluoride molecules, Phys. Rev. Lett. **127**, 033001 (2021).

[78] K. Blaum, J. Dilling, and W. Nörtershäuser, Precision atomic physics techniques for nuclear physics with radioactive beams, Phys. Scr. **2013**, 014017 (2013).

[79] P. Campbell, I. D. Moore, and M. R. Pearson, Laser spectroscopy for nuclear structure physics, Prog. Part. Nucl. Phys. **86**, 127 (2016).

[80] I. Angeli and K. Marinova, Table of experimental nuclear ground state charge radii: An update, At. Data Nucl. Data Tables **99**, 69 (2013).

[81] P.-G. Reinhard and W. Nazarewicz, Nuclear charge and neutron radii and nuclear matter: Trend analysis in Skyrme density-functional-theory approach, Phys. Rev. C **93**, 051303(R) (2016).

[82] C. Gorges, L. V. Rodríguez, D. L. Balabanski, M. L. Bissell, K. Blaum, B. Cheal, R. F. Garcia Ruiz, G. Georgiev, W. Gins, H. Heylen *et al.*, Laser spectroscopy of neutron-rich tin isotopes: A discontinuity in charge radii across the $n = 82$ shell closure, Phys. Rev. Lett. **122**, 192502 (2019).

[83] R. P. de Groote, J. Billowes, C. L. Binnersley, M. L. Bissell, T. E. Cocolios, T. Day Goodacre, G. J. Farooq-Smith, D. V. Fedorov, K. T. Flanagan, S. Franchoo *et al.*, Measurement and microscopic description of odd–even staggering of charge radii of exotic copper isotopes, Nat. Phys. **16**, 620 (2020).

[84] G. Barontini, L. Blackburn, V. Boyer, F. Butuc-Mayer, X. Calmet, J. R. Crespo López-Urrutia, E. A. Curtis, B. Darquié, J. Dunningham, N. J. Fitch *et al.*, Measuring the stability of fundamental constants with a network of clocks, EPJ Quantum Technol. **9**, 12 (2022).

[85] B. J. Drouin, C. E. Miller, H. S. Müller, and E. A. Cohen, The rotational spectra, isotopically independent parameters, and interatomic potentials for the $X\,\Pi_{3/2}$ and $X\,\Pi_{1/2}$ states of BrO, J. Mol. Spectrosc. **205**, 128 (2001).

[86] M. Doppelbauer, S. C. Wright, S. Hofsäss, B. G. Sartakov, G. Meijer, and S. Truppe, Hyperfine-resolved optical spectroscopy of the $A2\Pi \leftarrow X2\Sigma+$ transition in MgF, J. Chem. Phys. **156**, 134301 (2022).

[87] C. M. Holland, Y. Lu, and L. W. Cheuk, Synthesizing optical spectra using computer-generated holography techniques, New J. Phys. **23**, 033028 (2021).

[88] Y. Zeng, A. Jadbabaie, A. N. Patel, P. Yu, T. C. Steimle, and N. R. Hutzler, Optical cycling in polyatomic molecules with complex hyperfine structure, Phys. Rev. A **108**, 012813 (2023).

[89] R. Aiello, V. Di Sarno, M. G. Delli Santi, M. De Rosa, I. Ricciardi, P. De Natale, L. Santamaria, G. Giusfredi, and P. Maddaloni, Absolute frequency metrology of buffer-gas-cooled molecular spectra at 1 kHz accuracy level, Nat. Commun. **13**, 7016 (2022).

[90] S. Hofsäss, J. E. Padilla-Castillo, S. C. Wright, S. Kray, R. Thomas, B. G. Sartakov, B. Ohayon, G. Meijer, and S. Truppe, High-resolution isotope-shift spectroscopy of Cd I, Phys. Rev. Res. **5**, 013043 (2023).

[91] F. Kogel, Laser cooling of molecules for precision measurements of parity violation, Ph.D. thesis, University of Stuttgart, 2025.

[92] J. Brown and A. Carrington, *Rotational Spectroscopy of Diatomic Molecules*, Cambridge Molecular Science Series (Cambridge University Press, Cambridge, 2003).

[93] R. A. Frosch and H. M. Foley, Magnetic hyperfine structure in diatomic molecules, Phys. Rev. **88**, 1337 (1952).

[94] T. Chen, W. Bu, and B. Yan, Structure, branching ratios, and a laser-cooling scheme for the ^{138}BaF molecule, Phys. Rev. A **94**, 063415 (2016).

[95] Y. Hao, L. F. Pasteka, L. Visscher, P. Aggarwal, H. L. Bethlem, A. Boeschoten, A. Borschevsky, M. Denis, K. Esajas, S. Hoekstra *et al.*, High accuracy theoretical investigations of CaF, SrF, and BaF and implications for laser-cooling, J. Chem. Phys. **151**, 034302 (2019).

[96] M. Yeo, M. T. Hummon, A. L. Collopy, B. Yan, B. Hemmerling, E. Chae, J. M. Doyle, and J. Ye, Rotational state microwave mixing for laser cooling of complex diatomic molecules, Phys. Rev. Lett. **114**, 223003 (2015).

[97] A. L. Collopy, S. Ding, Y. Wu, I. A. Finneran, L. Anderegg, B. L. Augenbraun, J. M. Doyle, and J. Ye, 3D magneto-optical trap of yttrium monoxide, Phys. Rev. Lett. **121**, 213201 (2018).

[98] M. Auzinsh, D. Budker, and S. Rochester, *Optically Polarized Atoms* (Oxford University Press, Oxford, 2010).

[99] J. A. Devlin and M. R. Tarbutt, Laser cooling and magneto-optical trapping of molecules analyzed using optical Bloch equations and the Fokker-Planck-Kramers equation, Phys. Rev. A **98**, 063415 (2018).

[100] P. Aggarwal, V. R. Marshall, H. L. Bethlem, A. Boeschoten, A. Borschevsky, M. Denis, K. Esajas, Y. Hao, S. Hoekstra, K. Jungmann *et al.* (NL-eEDM Collaboration), Lifetime measurements of the $A^2\Pi_{1/2}$ and $A^2\Pi_{3/2}$ states in BaF, Phys. Rev. A **100**, 052503 (2019).